



Deposited via The University of Leeds.

White Rose Research Online URL for this paper:

<https://eprints.whiterose.ac.uk/id/eprint/229326/>

Version: Accepted Version

Article:

Naskar, S. and Pal, A. (2022) Effects of kinematic and magnetic boundary conditions on the dynamics of convection-driven plane layer dynamos. *Journal of Fluid Mechanics*, 951. A7. ISSN: 0022-1120

<https://doi.org/10.1017/jfm.2022.841>

© The Author(s), 2022. This article has been published in a revised form in <https://doi.org/10.1017/jfm.2022.841>. This version is free to view and download for private research and study only. Not for re-distribution or re-use.

Reuse

Items deposited in White Rose Research Online are protected by copyright, with all rights reserved unless indicated otherwise. They may be downloaded and/or printed for private study, or other acts as permitted by national copyright laws. The publisher or other rights holders may allow further reproduction and re-use of the full text version. This is indicated by the licence information on the White Rose Research Online record for the item.

Takedown

If you consider content in White Rose Research Online to be in breach of UK law, please notify us by emailing eprints@whiterose.ac.uk including the URL of the record and the reason for the withdrawal request.

Banner appropriate to article type will appear here in typeset article

1 **Effects of kinematic and magnetic boundary** 2 **conditions on the dynamics of convection-driven** 3 **plane layer dynamos.**

4 **Souvik Naskar¹, Anikesh Pal¹†**

5 ¹Department of Mechanical Engineering, Indian Institute of Technology, Kanpur 208016, India

6 (Received xx; revised xx; accepted xx)

7 Rapidly rotating convection-driven dynamos are investigated under different kinematic and
8 magnetic boundary conditions using direct numerical simulations (DNS). At a fixed rotation
9 rate, represented by the Ekman number $E = 5 \times 10^{-7}$, the thermal forcing is varied from 2 to
10 20 times its value at the onset of convection ($\mathcal{R} = Ra/Ra_c = 2-20$, where Ra is the Rayleigh
11 number), keeping the fluid properties constant ($Pr = Pr_m = 1$, where Pr and Pr_m are the
12 thermal and magnetic Prandtl numbers). The statistical behaviour of the dynamos, including
13 the force balance, energetics, and the heat transport, depends on the boundary conditions
14 that dictate both the boundary layer and the interior dynamics. At a fixed thermal forcing
15 ($\mathcal{R} = 3$), the horizontal and vertical velocities are higher with no-slip conditions compared
16 to free-slip conditions at the wall. The structure and strength of the magnetic field produced
17 by the dynamos, especially near the walls, depend on both velocity and magnetic boundary
18 conditions. Though the leading-order force balance in the bulk remains geostrophic, the
19 Lorentz force becomes comparable to Coriolis force inside the thermal boundary layer with
20 no-slip, electrically conducting conditions. In this case, a term signifying the work done
21 by the Lorentz force in the turbulent kinetic energy (t.k.e.) equation is found to have some
22 components that extract energy from the velocity field to produce magnetic field, while some
23 other components extract energy from the magnetic field to produce t.k.e. However, with no-
24 slip, pseudo-vacuum conditions, all the components of the work done by the Lorentz force,
25 perform unidirectional energy transfer to produce magnetic energy from the kinetic energy
26 of the fluid to sustain dynamo action. We find heat transfer enhancement in the rotating
27 dynamo convection (DC), as compared with non-magnetic rotating convection (RC), for all
28 investigated combination of boundary conditions, with the peak enhancement lying in the
29 range $\mathcal{R} = 3 - 4$. For free-slip conditions, in the absence of an Ekman layer, the dynamo
30 action may alter the heat transport significantly by suppressing the formation of large-scale
31 vortices (LSV). However, the highest heat transfer enhancement is found at $\mathcal{R} = 3$ with
32 no-slip, electrically conducting walls, which can be attributed to a local magnetorelaxation
33 of the rotational constraint due to enhanced Lorentz force inside the thermal boundary layer.

34 **Key words:**

† Email address for correspondence: pala@iitk.ac.in
Cambridge University Press

2

35 1. Introduction

36 The geomagnetic field acts as a shield to protect us from solar wind (Tarduno 2018) apart
37 from directly influencing the atmosphere (Cnossen 2014), biology and evolution of life on
38 Earth (Erdmann *et al.* 2021). Such magnetic fields of planets and stars are known to be
39 generated by a dynamo mechanism driven by the convection of electrically conducting fluids
40 (Rüdiger & Hollerbach 2006). In this self-sustained dynamo mechanism, the convective
41 motion of electrically conducting fluids leads to the amplification of a small magnetic
42 perturbation by electromagnetic induction. The induced magnetic field is then maintained
43 against Joule dissipation by continuously converting some of the kinetic energy of the fluid
44 to magnetic energy. A simple model of such dynamos is the Rayleigh-Bénard convection
45 (RBC) in a plane layer between two parallel plates, heated from the bottom and cooled
46 from the top, permeated by a magnetic field. Inclusion of global rotation in such flows can
47 break the reflectional symmetry of the convection to induce large-scale magnetic fields
48 (Moffatt & Dormy 2019; Tobias 2021). Non-magnetic RC has been studied extensively using
49 experiments (King *et al.* 2009; Stellmach *et al.* 2014; Kunnen *et al.* 2010; Ecke & Niemela
50 2014; King & Aurnou 2013; Aurnou *et al.* 2018; Cheng *et al.* 2020), DNS (Guzmán *et al.*
51 2021; Guervilly *et al.* 2017; Kunnen *et al.* 2016; Schmitz & Tilgner 2010; Weiss *et al.* 2010;
52 Stellmach *et al.* 2014; Cheng *et al.* 2015), and reduced-order asymptotic models (Julien *et al.*
53 2012*a,b*; Rubio *et al.* 2014; Nieves *et al.* 2014; Julien *et al.* 2016; Plumley *et al.* 2016, 2017;
54 Maffei *et al.* 2021) to investigate the transport properties, force balance and flow structures.
55 However, dynamical balances and heat transport in rotating DC have received less attention.
56

57 The flow and thermal field characteristics in a plane layer RC serve as a classical
58 framework for studying solar and planetary convection apart from deep convection in
59 terrestrial oceans (Julien *et al.* 1996). Here, the convection depends primarily on the thermal
60 forcing, the rotation rate, and the fluid properties represented by the Rayleigh number (Ra),
61 the Ekman number (E), and the Prandtl number (Pr), respectively (as defined in section
62 2). The convection begins with steady cellular patterns when the thermal forcing exceeds a
63 critical Rayleigh number (Ra_c), which scales as $E^{-4/3}$ for $Pr > 0.67$ in the limit of large
64 rotation rates, $E \rightarrow 0$ (Chandrasekhar 1961). This scaling leads to higher Ra_c compared
65 to non-rotating RBC, depicting the stabilizing action of the Coriolis force. Increasing
66 the thermal forcing at a fixed rotation rate gives rise to distinct convection regimes with
67 separate flow phenomenology and scaling of the transport properties. The flow regimes
68 are classified as (i) rotation dominated convection, (ii) rotation affected convection, and
69 (iii) rotation unaffected convection, depending on the relative importance of the Coriolis
70 force in the dynamical balance and heat transfer. The rotation dominated convection regime
71 is characterized by a geostrophic balance between Coriolis and pressure forces, whereas
72 inertial effects break this balance in the rotation affected convection regime at higher
73 thermal forcing. The dependence on the rotation rate is diminished at even higher forcing
74 for rotation unaffected regime with heat transfer behaviour similar to RBC (see Kunnen
75 (2021) for details). Even the rotation dominated geostrophic convection regime can be
76 divided into sub-regimes with distinct flow structures such as (in the order of increasing
77 thermal forcing) cells, transient Taylor columns, plumes, and large scale vortices (LSV) in
78 geostrophic turbulence (Julien *et al.* 2012*b*; Nieves *et al.* 2014; Kunnen *et al.* 2016). Most
79 of these flow features have been confirmed by laboratory experiments in rotating cylinders
80 (Cheng *et al.* 2015; Kunnen *et al.* 2010). In the simulations, the flow features may also
81 depend on the boundary conditions imposed on the plates. For example, LSV formation in
82 geostrophic turbulence is shifted to higher rotation rates with no-slip boundary conditions
83 as compared to the free-slip boundary conditions at a fixed thermal forcing (Guzmán *et al.*

84 2020), as no-slip boundaries can suppress the formation (Stellmach *et al.* 2014; Kunnen
85 *et al.* 2016). Though the regime transition with thermal forcing is found to be independent
86 of boundary conditions (Kunnen *et al.* 2016), the force balance and heat transport behaviour
87 in RC depends on the kinematic boundary conditions.

88

89

The classical RBC between parallel plates can be separated in two regions: (i) the boundary
90 layer regions with high thermal and velocity gradients near the plates, and (ii) the well-mixed
91 bulk region in the interior. In the absence of rotation, the heat transport is throttled by the
92 presence of boundary layers, with the Nusselt number (Nu , a non-dimensional measure of
93 heat transfer defined in equation 2.10) scaling as $Ra^{1/3}$ with the thermal forcing (Plumley
94 & Julien 2019; Iyer *et al.* 2020). The thermal behaviour of plane layer RC in the rotation-
95 dominated regime is diametrically opposite, with the bulk rather than the boundary layer
96 constraining the convective heat transport. For large rotation rates ($E \rightarrow 0$) the heat transfer
97 should follow the diffusion free scaling $Nu \sim Ra^{3/2}$ irrespective of the boundary conditions
98 (Julien *et al.* 2012a). Experimental difficulties of maintaining turbulence at small E , and the
99 computational challenges pertaining to the spatio-temporal resolution requirement restrict
100 the demonstration of this scaling in a laboratory or DNS with no-slip boundaries. Instead,
101 the Ekman pumping near the thin boundary layers significantly enhances the heat transport
102 even at low Ekman numbers $E \approx 10^{-8}$ (Kunnen *et al.* 2010; Stellmach *et al.* 2014). This
103 results in a steeper heat transport scaling $Nu \sim Ra^3$, when no-slip conditions are used
104 rather than free-slip conditions at the boundaries. Reduced-order models with parameterized
105 Ekman pumping corroborate these scaling predictions (Stellmach *et al.* 2014; Plumley
106 *et al.* 2017, 2016). The presence of no-slip walls, with the associated Ekman pumping
107 effect, can significantly enhance vertical velocities, even in the interior, because of the
108 enhanced momentum flux from the boundary towards the bulk. The viscous and inertial
109 force magnitudes near the walls also increase by one order of magnitude compared to their
110 bulk values near the no-slip boundaries leading to increased ageostrophy (Guzmán *et al.*
111 2021).

112

113

Motivated by the boundary layer effects on plane layer RC, we intend to investigate the
114 boundary layer dynamics in DC under different combinations of kinematic and magnetic
115 boundary conditions. For rotating DC, the magnetic Prandtl number (Pr_m) appears as an
116 extra parameter that decides the growth and saturation of the magnetic field (Tobias *et al.*
117 2012; Tobias 2021). Such plane layer convection of electrically conducting fluids was shown
118 to induce dynamo action in early analytical (Childress & Soward 1972; Soward 1974;
119 Fautrelle & Childress 1982) and numerical studies (Meneguzzi & Pouquet 1989). Using
120 this plane layer model with no-slip and perfectly conducting boundaries, St Pierre (1993)
121 demonstrated subcritical dynamo action at $E = 5 \times 10^{-6}$ with the magnetic field concentrated
122 near the plates. Thelen & Cattaneo (2000) studied the effect of **perfectly conducting, perfectly**
123 **insulating, and pseudo-vacuum** magnetic boundary conditions on dynamo action. These
124 boundary conditions were found to dictate the strength and structure of the magnetic field
125 near the plates, though the bulk behaviour was independent of the boundary conditions.
126 Stellmach & Hansen (2004) used free-slip, electrically conducting boundaries to study
127 rapidly rotating ($E = 2 \times 10^{-4} - 10^{-6}$), weakly non-linear DC and reported strongly
128 time-dependent flow and magnetic field behaviour with cyclic variation between small and
129 large-scale structures. These particular boundary conditions facilitate comparison of the
130 dynamo behaviour with analytical models (Childress & Soward 1972; Soward 1974). They
131 reported strongly time-dependent flow and magnetic field behaviour with cyclic variation
132 between small and large-scale structures. Tilgner (2012, 2014) reported a transition between
133 large-scale field generation governed by flow helicity to small-scale field generation driven

4

134 by field stretching. The transition happens at $Re_m E^{1/3} \approx 13.5$ (where Re_m is the magnetic
 135 Reynolds number signifying the relative strength of electromagnetic induction over ohmic
 136 diffusion), for electrically conducting boundaries irrespective of the kinematic condition
 137 (no-slip or free-slip). Large-scale vortex driven dynamos were demonstrated by Guervilly
 138 *et al.* (2015, 2017), that generated large-scale magnetic field. In the absence of a magnetic
 139 field, these vortices lead to the reduction of heat transfer between the plates (Guervilly *et al.*
 140 2014). However small-scale magnetic field may suppress the formation of LSV at sufficiently
 141 high $Re_m \gtrsim 550$ (Guervilly *et al.* 2017). Interestingly, Yan & Calkins (2022*b*) has recently
 142 demonstrated the existence of large-scale fields in rapidly rotating DC with a dominant mean
 143 magnetic field for $Re_m E^{1/3} \lesssim O(1)$, without the presence of large flow helicity or LSV.
 144 Asymptotically reduced DC models (vanishingly small inertia and viscous forces with respect
 145 to the Coriolis force), with a leading-order geostrophic balance, was studied by Calkins
 146 *et al.* (2015), revealing four distinct dynamo regimes with separate scaling for the magnetic
 147 to kinetic energy density ratios (Calkins 2018). RBC driven dynamos have been studied by
 148 Yan *et al.* (2021), who reported heat transfer scaling similar to non-rotating convection. Yan
 149 & Calkins (2022*a*) has reported the force balance, heat transport and scaling of the flow
 150 properties in rapidly rotating DC with free-slip, electrically conducting boundary conditions.
 151 The scaling of the transport properties was found to be consistent with the asymptotic theory
 152 of Calkins *et al.* (2015); Calkins (2018). Recently, Kolhey *et al.* (2022) has studied the effect
 153 of thermal, kinematic and magnetic boundary conditions in DC in the geostrophic turbulent
 154 regime. The magnetic field topology was found to depend on the choice of magnetic
 155 boundary conditions. Nevertheless, the dependence of the heat transfer, force balance and
 156 energetics on the boundary conditions for varying flow regimes remains open for exploration.
 157

158 In the present study, we perform DNS of convection-driven dynamos, in the rotation-
 159 dominated regime, with varying thermal forcing subjected to different boundary conditions.
 160 Our simulations of plane layer RC, with no-slip and free-slip kinematic boundary conditions,
 161 serve as references to study the dynamo behaviour at four combinations of boundary
 162 conditions (combinations of no-slip or free-slip as velocity boundary conditions with
 163 perfectly conducting or pseudo-vacuum magnetic boundary conditions). The statistical
 164 characteristics of the dynamo, along with the existing force balance in the system, are found
 165 to depend on the kinematic and magnetic boundary conditions, both in the bulk and in the
 166 boundary layer region. Heat transfer behaviour was also found to be strongly dependent on
 167 the imposed conditions at the plates. The governing equations with the boundary conditions
 168 are detailed in section 2. The statistical behaviour of the flow and magnetic field is presented
 169 in section 3.1. In sections 3.2 and 3.3 we present the force balance and energy budget in the
 170 dynamos. Finally, we look into the heat transport behaviour in section 3.4 and summarize
 171 our findings in section 4.
 172

173 2. Method

174

2.1. Governing Equations

175 In the present study, rapidly rotating DC in a three-dimensional Cartesian layer of incom-
 176 pressible, electrically conducting, Boussinesq fluid is considered. The horizontal layer is
 177 kept between two parallel plates with a distance d and temperature difference ΔT , where the
 178 lower plate is hotter than the upper plate. The system rotates with a constant angular velocity
 179 $\boldsymbol{\Omega} = \Omega \hat{e}_3$ about the vertical axis, anti-parallel to the gravity $\mathbf{g} = -g \hat{e}_3$. The electrically
 180 conducting Newtonian fluid has density ρ , kinematic viscosity ν , thermal diffusivity κ ,

Cambridge University Press

Focus on Fluids articles must not exceed this page length

181 adiabatic volume expansion coefficient α , magnetic permeability μ , electrical conductivity
 182 σ and the magnetic diffusivity (η). The layer depth d and temperature difference ΔT is the
 183 natural choice for length and temperature scales, whereas, $u_f = \sqrt{g\alpha\Delta T d}$, and $\sqrt{\rho\mu}u_f$
 184 are chosen to be the velocity (Guzmán *et al.* 2021) and magnetic field scales. The non-
 185 dimensional governing equations for the velocity field u_i , temperature field θ , and magnetic
 186 field B_i are expressed as the following.

$$187 \quad \frac{\partial u_j}{\partial x_j} = \frac{\partial B_j}{\partial x_j} = 0, \quad (2.1)$$

$$190 \quad \frac{\partial u_i}{\partial t} + u_j \frac{\partial u_i}{\partial x_j} = -\frac{\partial p}{\partial x_i} + \frac{1}{E} \sqrt{\frac{Pr}{Ra}} \epsilon_{ij3} u_j \hat{e}_3 + B_j \frac{\partial B_i}{\partial x_j} + \theta \delta_{i3} + \sqrt{\frac{Pr}{Ra}} \frac{\partial^2 u_i}{\partial x_j \partial x_j}, \quad (2.2)$$

$$192 \quad \frac{\partial \theta}{\partial t} + u_j \frac{\partial \theta}{\partial x_j} = \frac{1}{\sqrt{RaPr}} \frac{\partial^2 \theta}{\partial x_j \partial x_j}, \quad (2.3)$$

$$194 \quad \frac{\partial B_i}{\partial t} + u_j \frac{\partial B_i}{\partial x_j} = B_j \frac{\partial u_i}{\partial x_j} + \sqrt{\frac{Pr}{Ra}} \frac{1}{Pr_m} \frac{\partial^2 B_i}{\partial x_j \partial x_j}. \quad (2.4)$$

195 The definitions of the four non-dimensional parameters, namely Rayleigh number (Ra),
 196 Ekman number (E), thermal and magnetic Prandtl numbers (Pr and Pr_m) are given as
 197 follows.

$$198 \quad Ra = \frac{g\alpha\Delta T d^3}{\kappa\nu}, \quad E = \frac{\nu}{2\Omega d^2}, \quad Pr = \frac{\nu}{\kappa}, \quad Pr_m = \frac{\nu}{\eta}. \quad (2.5)$$

199 In the horizontal directions (x_1, x_2) periodic boundary conditions are applied. As we aim
 200 to study the effect of Ekman layer dynamics on the dynamo convection, both no-slip and
 201 free-slip boundary conditions are implemented in the vertical direction (x_3) as the following.

$$203 \quad \begin{aligned} u_1 = u_2 = u_3 = 0 \text{ at } x_3 = \pm 1/2 & \quad (\text{no-slip}) \\ \frac{\partial u_1}{\partial x_3} = \frac{\partial u_2}{\partial x_3} = 0, u_3 = 0 \text{ at } x_3 = \pm 1/2 & \quad (\text{free-slip}). \end{aligned} \quad (2.6)$$

204 Isothermal boundary conditions with unstable temperature gradient are imposed to drive
 205 convection as follows.

$$207 \quad \theta = 1/2 \text{ at } x_3 = -1/2, \quad \theta = -1/2 \text{ at } x_3 = 1/2 \quad (2.7)$$

208 For the magnetic field, both perfectly conducting and pseudo-vacuum conditions are
 209 implemented to compare the resulting magnetic field structure. For perfectly conducting
 210 boundary the field is constrained to be horizontal at the wall (Cattaneo & Hughes 2006).
 211 **The pseudo-vacuum conditions (Thelen & Cattaneo 2000; Kolhey *et al.* 2022) are used to**
 212 **approximate insulating conditions (Jones & Roberts 2000) where the field is purely vertical**
 213 **at the boundaries.**

$$215 \quad \begin{aligned} \frac{\partial B_1}{\partial x_3} = \frac{\partial B_2}{\partial x_3} = B_3 = 0 \text{ at } x_3 = \pm 1/2 & \quad (\text{conducting}) \\ B_1 = B_2 = \frac{\partial B_3}{\partial x_3} = 0 \text{ at } x_3 = \pm 1/2 & \quad (\text{pseudo-vacuum}) \end{aligned} \quad (2.8)$$

\mathcal{R}	\widetilde{Ra}	Ro_C	Re_m	Λ_{tr}	Λ_V	Λ_T	\overline{M}/M	Nu/Nu_0	$\frac{\langle \epsilon_v \rangle}{\langle \epsilon_0 \rangle}$	$\frac{\langle \epsilon_j \rangle}{\langle \epsilon \rangle}$	$\langle \mathcal{B} \rangle^*$	$-\langle \epsilon \rangle^*$	τ	τ_0
2	15.2	0.031	729	0.109	0.038	0.005	0.3994	0.73	0.50	0.32	0.562	0.542	1.171	-
2.5	19.0	0.035	1327	0.258	0.011	0.292	0.0603	1.26	0.94	0.34	1.955	1.934	1.027	-
3	22.8	0.038	2012	0.516	0.071	0.617	0.0040	1.72	1.44	0.36	3.566	3.459	0.933	-
4	30.4	0.044	2284	0.842	0.087	0.555	0.0033	1.49	1.23	0.38	3.737	3.694	0.848	-
5	38.0	0.049	2660	1.199	0.129	0.462	0.0029	1.43	1.08	0.39	3.675	3.661	0.827	-
10	76.0	0.069	4203	1.871	0.132	0.214	0.0006	1.17	0.85	0.34	3.902	3.818	0.784	-
20	152.0	0.098	7642	6.643	0.183	0.167	0.0003	1.14	0.82	0.39	5.141	4.980	0.930	-

Table 1: Statistics of the dynamo simulations with NSC boundary conditions.

\mathcal{R}	\widetilde{Ra}	Ro_C	Re_m	Λ_{tr}	Λ_V	Λ_T	\overline{M}/M	Nu/Nu_0	$\frac{\langle \epsilon_v \rangle}{\langle \epsilon_0 \rangle}$	$\frac{\langle \epsilon_j \rangle}{\langle \epsilon \rangle}$	$\langle \mathcal{B} \rangle^*$	$-\langle \epsilon \rangle^*$	τ	τ_0
2	15.2	0.031	682	0.295	0.009	0.011	0.1617	0.95	0.69	0.40	0.754	0.724	1.302	1.058
2.5	19.0	0.035	1403	0.311	0.044	0.043	0.0043	1.00	1.20	0.20	1.529	1.516	1.072	1.071
3	22.8	0.038	2044	0.439	0.095	0.097	0.0015	1.41	1.26	0.25	2.901	2.969	1.034	1.046
4	30.4	0.044	2212	0.889	0.055	0.112	0.0008	1.24	0.95	0.36	3.063	3.050	0.903	0.986
5	38.0	0.049	2491	1.063	0.038	0.159	0.0007	1.23	0.92	0.36	3.153	3.131	0.816	0.958
10	76.0	0.069	3748	2.934	0.033	0.269	0.0006	1.10	0.71	0.42	3.670	3.548	0.735	1.102 [#]
20	152.0	0.098	6422	7.995	0.021	0.371	0.0005	1.09	0.82	0.41	6.185	6.042	0.707	1.341 [#]

Table 2: Statistics of the dynamo simulations with NSV boundary conditions.

\mathcal{R}	\widetilde{Ra}	Ro_C	Re_m	Λ_{tr}	Λ_V	Λ_T	\overline{M}/M	Nu/Nu_0	$\frac{\langle \epsilon_v \rangle}{\langle \epsilon_0 \rangle}$	$\frac{\langle \epsilon_j \rangle}{\langle \epsilon \rangle}$	$\langle \mathcal{B} \rangle^*$	$-\langle \epsilon \rangle^*$	τ	τ_0
2	17.4	0.033	641	0.218	0.001	0.001	0.1853	0.98	0.98	0.07	0.345	0.343	1.174	1.351
2.5	21.7	0.037	950	0.326	0.002	0.003	0.0173	1.00	0.97	0.03	0.524	0.520	1.234	1.350
3	26.1	0.041	1176	0.437	0.003	0.005	0.0061	1.08	1.02	0.01	0.585	0.581	1.171	1.414
4	34.8	0.047	2087	0.503	0.004	0.006	0.0020	1.44	1.04	0.34	1.812	1.753	1.019	2.960 [#]
5	43.5	0.052	2562	0.744	0.005	0.013	0.0019	1.42	1.02	0.35	2.248	2.162	0.953	3.054 [#]
10	87.0	0.074	3957	2.072	0.007	0.037	0.0018	1.02	0.74	0.39	2.883	2.718	0.825	7.755 [#]
20	174.0	0.105	7249	6.570	0.009	0.091	0.0008	0.98	0.73	0.42	4.482	4.261	0.802	4.050 [#]

Table 3: Statistics of the dynamo simulations with FSC boundary conditions.

\mathcal{R}	\widetilde{Ra}	Ro_C	Re_m	Λ_{tr}	Λ_V	Λ_T	\overline{M}/M	Nu/Nu_0	$\frac{\langle \epsilon_v \rangle}{\langle \epsilon_0 \rangle}$	$\frac{\langle \epsilon_j \rangle}{\langle \epsilon \rangle}$	$\langle \mathcal{B} \rangle^*$	$-\langle \epsilon \rangle^*$	τ	τ_0
2	17.4	0.033	460	0.026	0.027	0.017	0.0125	0.64	0.86	0.36	0.336	0.336	2.661	-
2.5	21.7	0.037	1056	0.034	0.030	0.019	0.0066	0.99	0.98	0.31	0.521	0.519	1.395	-
3	26.1	0.041	1414	0.047	0.036	0.019	0.0033	1.34	1.23	0.38	0.759	0.754	1.289	-
4	34.8	0.047	1858	0.999	0.043	0.029	0.0014	1.26	0.65	0.44	1.485	1.392	0.980	-
5	43.5	0.052	2311	2.0726	0.107	0.044	0.0013	1.23	0.64	0.50	2.101	1.995	0.886	-
10	87.0	0.074	3475	57.122	1.187	0.186	0.0011	1.19	0.32	0.78	4.323	4.192	0.917	-
20	174.0	0.105	6332	99.573	1.367	0.305	0.0009	1.13	0.33	0.72	5.766	5.712	0.848	-

Table 4: Statistics of the dynamo simulations with FSV boundary conditions. In the tables 1-4, \widetilde{Ra} is the reduced Rayleigh number and Ro_C is the convective Rossby number. Λ_{tr} is the traditional definition of Elsasser number, whereas Λ_V is the volume-averaged Elsasser number. Λ_T is the Elsasser number at the thermal boundary layer edge. Re_m is the magnetic Reynolds number. Nu/Nu_0 and $\langle \epsilon_v \rangle / \langle \epsilon_0 \rangle$ are the Nusselt number ratio and viscous dissipation ratio. $\langle \epsilon_j \rangle / \langle \epsilon \rangle$ is the ratio of Joule dissipation to the total dissipation.

The buoyancy flux $\langle \mathcal{B} \rangle^* = \langle u_3 \theta \rangle \times 10^4$ and total dissipation $\langle \epsilon \rangle^* = \langle \epsilon_v + \epsilon_j \rangle \times 10^4$ depicts the overall balance of energy. τ is the kinetic energy ratio indicating presence of LSV. Subscript "0" represents the properties for non-magnetic RC simulations. Such RC simulations with LSV are indicated by # in the last column.

216

2.2. Simulation Details

217 The governing equations 2.1-2.4 are solved in a cubic domain with a unit side length, using a
 218 finite difference method. The geometrical details and numerical algorithms are presented in
 219 Naskar & Pal (2022). We perform all the simulations at constant rotation rate and constant
 220 fluid properties by varying the thermal forcing and boundary conditions. The thermal forcing
 221 is represented by the convective supercriticality $\mathcal{R} = Ra/Ra_c$, where Ra_c is the minimum
 222 value of Ra required to start steady RC (Chandrasekhar 1961). In this study, we have used
 223 the values of critical Rayleigh number for non-magnetic convection as $Ra_c = 8.6E^{-4/3}$ for
 224 free-slip (Chandrasekhar 1961) and $Ra_c = 7.6E^{-4/3}$ for no-slip boundaries (King *et al.*
 225 2012; Kunnen 2021). We choose the values of $\mathcal{R} = (2, 2.5, 3, 4, 5, 10, 20)$, Ekman number
 226 $E = 5 \times 10^{-7}$ and the Prandtl numbers $Pr = Pr_m = 1$ for the present simulations. To investigate
 227 dynamo action for different boundary conditions, we perform six simulations at each value
 228 of \mathcal{R} : (a) non-magnetic RC with no-slip (NS) and free-slip (FS) boundary conditions, and
 229 (b) rotating DC subjected to the combinations kinematic (no-slip or free-slip) and magnetic
 230 (conducting or pseudo-vacuum) boundary conditions abbreviated as NSC, FSC, NSV and
 231 FSV. The simulation inputs and diagnostic parameters are summarized in tables 1-4. The
 232 computational domain, with an aspect ratio of unity, is about 26 times larger than the critical
 233 wavelength at the onset of RC ($\lambda_c = 4.8158E^{1/3}$) in the horizontal directions (Chandrasekhar
 234 1961). Therefore, we can ensure the statistical convergence of all the diagnostic properties
 235 (Yan & Calkins 2022a) presented in tables 1-4. A mesh with $1024 \times 1024 \times 256$ grid points is
 236 used for all the simulations, with uniform spacing in the horizontal and grid clustering in the
 237 vertical direction to resolve the boundary layers. The solver has been extensively validated
 238 for studies on rotating stratified flow (Pal & Chalamalla 2020), and various transitional and
 239 turbulent shear flows (Pal 2020; Pal & Sarkar 2015; Pal *et al.* 2013; Brucker & Sarkar
 240 2010). Details of the grid resolution and validation studies are reported in a previous study
 241 (Naskar & Pal 2022). The scaled values of the buoyancy flux, $\langle \mathcal{B} \rangle^* = \langle u_3 \theta \rangle \times 10^4$ and the
 242 total dissipation $\langle \epsilon \rangle^* = \langle \epsilon_v + \epsilon_j \rangle \times 10^4$ in tables 1-4 indicate sufficient resolution for all
 243 the simulations, as the grid can capture most of the energetic scales. It should be noted that
 244 the combination of the non-dimensional numbers appearing before the Coriolis term in the
 245 momentum equation 2.2 is the inverse of convective Rossby number $Ro_C = E(Ra/Pr)^{1/2}$
 246 frequently used in the literature on rapid RC (Aurnou *et al.* 2020). For all our simulations,
 247 the convective Rossby number $Ro_C \ll 1$ indicates rapid RC regime, as shown in tables 1-4.
 248 The reduced Rayleigh number $\widetilde{Ra} = RaE^{4/3}$ is another important parameter presented in
 249 these tables to compare against the literature on rapid RC (Julien *et al.* 2012a; King *et al.*
 250 2012; Calkins 2018).

251

2.3. Turbulence statistics

252 For moderate to high $Re_m \geq O(10 - 100)$, the system can induce its own magnetic field
 253 with a wide range of length and time scales. In such cases, it is worthwhile to decompose
 254 the magnetic field into mean and fluctuating parts following the developments in mean-field
 255 electrodynamics (Cattaneo & Hughes 2006). Therefore, we perform Reynolds decomposition
 257 on all the variables such that

$$\begin{aligned}
 \phi(x, y, z, t) &= \bar{\phi}(z, t) + \phi'(x, y, z, t) \\
 \bar{\phi}(z, t) &= \int_{A_h} \phi(x, y, z, t) dx dy
 \end{aligned}
 \tag{2.9}$$

258

259 Here, A_h is the horizontal area of integration of the flow variables $\phi = \{u_i, p, \theta, B_i\}$. The
 260 root mean square (r.m.s.) values are calculated as $\phi_{rms} = (\overline{\phi^2})^{1/2}$. The energy budget for

8

261 the t.k.e. (K), as derived from the momentum equation 2.2 by utilizing 2.9, is presented in
 262 Appendix A.

263

264 We compare our simulations in terms of the heat transfer, represented by the Nusselt
 265 number (Nu). This is defined as the ratio of total heat flux to the conductive heat flux
 266 transferred from the bottom plate to the top plate.

$$268 \quad Nu = \frac{qd}{k\Delta T} = 1 + \sqrt{RaPr}\langle\mathcal{B}\rangle \quad (2.10)$$

269 Here. $\langle\phi\rangle = \int_0^1 \bar{\phi} dx_3$ denote average over the entire volume, q represents the total heat
 270 flux and \mathcal{B} stands for the vertical buoyancy flux (see A 2). Subscript "0" is used to represent
 271 the properties without magnetic field (NS and FS cases) in the rest of this paper. All the
 272 statistics presented here are averaged in time for at least 100 free-fall time units d/u_f , after
 273 the simulations settle in a statistically stationary state.

274 3. Result

275 Naskar & Pal (2022) performed DNS of rapidly rotating dynamos with no-slip boundary
 276 conditions and reported a significant enhancement (72%) in heat transfer as compared to
 277 non-magnetic RC at $\mathcal{R} = 3$. An increase in the Lorentz force near the boundaries was found to
 278 be the reason for this enhanced heat transport. Owing to this interesting behaviour, we study
 279 the statistical details, force balance and energy budget of the dynamos at $\mathcal{R} = 3$ subjected to
 280 different boundary conditions. To further understand the changes in the dynamo behaviour
 281 with \mathcal{R} , we have tabulated the volume-averaged statistics in tables 1-4.

282

3.1. Statistical details of the dynamos

283 In this section, we discuss the statistical behaviour of the velocity, temperature, and magnetic
 284 field of the dynamos subjected to different boundary conditions at $\mathcal{R} = 3$. In figure 1a, the
 285 r.m.s. horizontal velocity is presented. To clarify the near-wall variation, we have included
 286 a magnified inset. At this point, it is important to distinguish between the well-mixed
 287 bulk region in the interior and the boundary layer region with high gradients near the
 288 plates. Therefore, we define the thermal boundary layer as the region near the plates where
 289 temperature gradients are high, and its thickness (δ_T) is evaluated as the distance from
 290 the wall, where the r.m.s. value of temperature reaches a maximum (King *et al.* 2009).
 291 Furthermore, when the no-slip condition is imposed, the viscous effects are confined within
 292 a thin Ekman layer, defined as the distance of the maximum of the horizontal r.m.s. velocity
 293 from the wall, δ_E . The edge of the Ekman boundary layer for the no-slip cases at $x_3 = -0.498$,
 294 as marked with a horizontal red dashed line in the inset in figure 1a, remains independent
 295 of the magnetic boundary conditions. In figure 1a, the horizontal velocity in the bulk for
 296 NS and NSC cases overlap, whereas the profiles inside the Ekman layer are independent of
 297 magnetic boundary conditions. For the no-slip boundary condition, the horizontal velocity
 298 can be seen to be higher than that of the free-slip boundaries, both in the bulk and near the
 299 boundaries. A similar behaviour is observed for the r.m.s. vertical velocity and temperature
 300 fluctuations in figure 1b and c respectively. The vertical variation of the r.m.s. velocities
 301 can be understood from the Ekman pumping mechanism (Guzmán *et al.* 2021). The velocity
 302 magnitudes around a plume site, as depicted in figure 2, can provide further insight into
 303 this phenomenon. Here, the conical plume sites can be recognized from the temperature
 304 isosurface $\theta = 0.45$ near the lower boundary in figure 2a. The horizontal convergence (or
 305 divergence) of fluid at the sites of the vortical plumes (figure 2b) enhances the horizontal

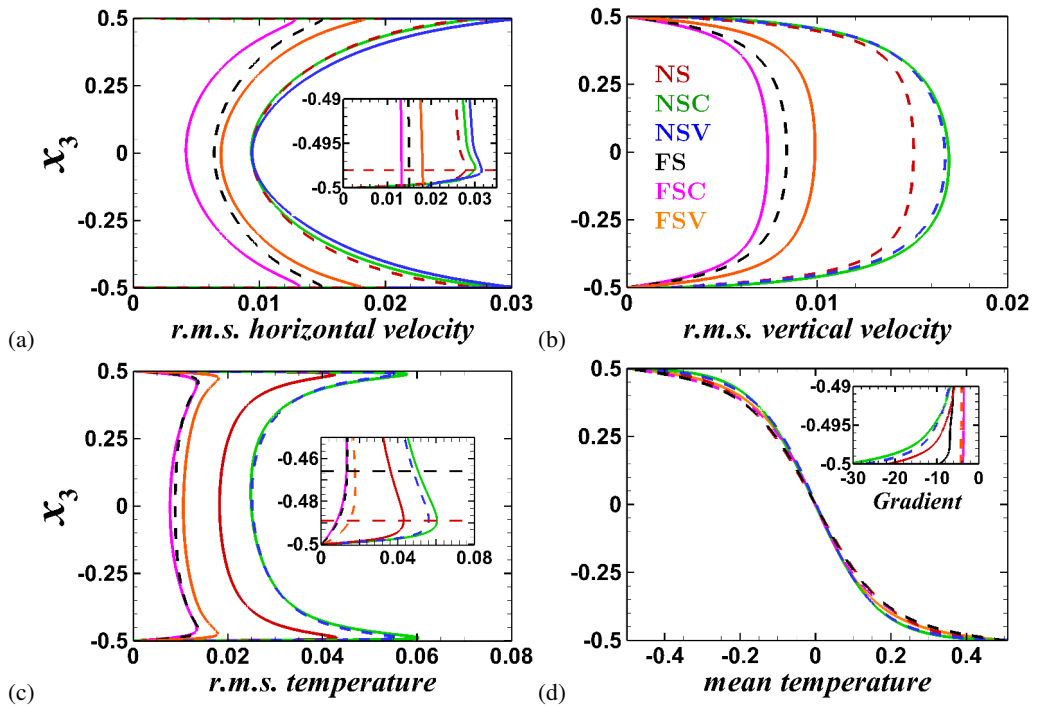


Figure 1: Vertical variation of the r.m.s. quantities: (a) horizontal velocity, $u_{1,r.m.s.}$ (b) vertical velocity, $u_{3,r.m.s.}$ (c) r.m.s. temperature, $\theta_{r.m.s.}$ (d) mean temperature θ at $\mathcal{R} = 3$. All the quantities are averaged in time and in the horizontal directions. Dashed lines are used as needed for improving the clarity of the plots.

306 velocity near the wall with the no-slip boundary condition compared to the free-slip cases
 307 in figure 1a. This fluid then gains vertical acceleration towards the bulk, resulting in higher
 308 vertical velocities (figure 2c), as plotted in figure 1b. Ekman pumping induced by the no-slip
 309 boundaries is known to enhance momentum and heat transport (Stellmach *et al.* 2014), and is
 310 the reason for the enhanced r.m.s. velocities and temperature fluctuations, especially near the
 311 boundaries. Furthermore, in the inset of figure 1c, the thermal boundary layer thickness (δ_T)
 312 for the free-slip boundaries (horizontal black dashed line) is about three times higher than
 313 the no-slip boundaries (horizontal red dashed line). The thermal fluctuations are enhanced
 314 with no-slip boundary conditions, with maximum r.m.s. fluctuation shifting towards the
 315 wall. It is noteworthy that changing the boundary conditions can significantly modulate the
 316 bulk behaviour apart from the boundary layer dynamics. Also, the effects of changing the
 317 kinematic boundary condition on the velocity and thermal fields are more prominent than
 318 the magnetic conditions. The mean temperature profile shows a higher temperature gradient
 319 near the bottom wall for no-slip conditions (see the inset in figure 1d), with the highest
 320 vertical gradient for the NSC case indicating the highest heat transfer from the wall among all
 321 the cases at $\mathcal{R} = 3$ (see section 3.4 for detailed discussion). However, the mean temperature
 322 profile and its gradient at the mid-plane remain nearly independent of boundary conditions.
 323 The magnetic Reynolds number $Re_m = RePr_m = u_\tau d/\eta$, (where $u_\tau = u_f \langle 2K \rangle^{1/2}$ is the
 324 turbulent velocity scale), has the same value with the Reynolds number Re , for $Pr_m = 1$
 325 in the present simulations (see tables 1-4). The Reynolds number increases by an order
 326 of magnitude in the range $\mathcal{R} = 2 - 20$, indicating increased velocity fluctuations with
 327 thermal forcing, irrespective of boundary conditions. The r.m.s. temperature fluctuations

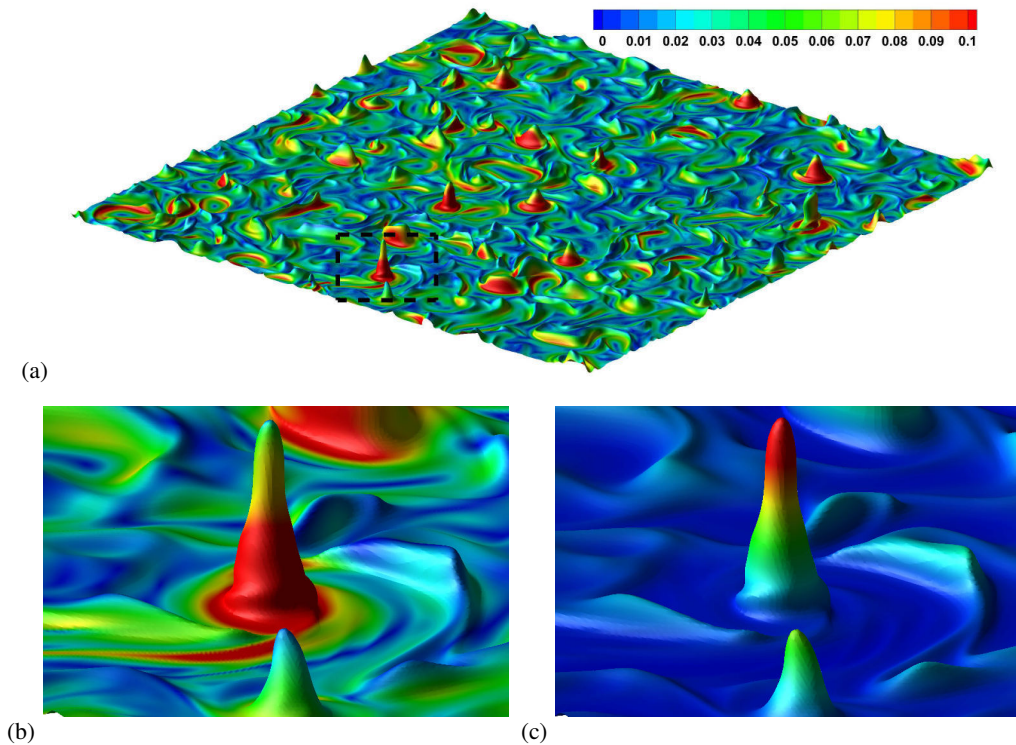


Figure 2: (a) Plume sites visualized by an isosurface of the instantaneous temperature field with $\theta = 0.45$, colored by the horizontal velocity for NSC case at $\mathcal{R} = 3$. A typical plume site in (a), as marked by dashed rectangle, has been magnified and colored by horizontal and vertical velocities in figures (b) and (c) respectively.

328 also increase monotonically with increased thermal forcing (figure not presented). The
 329 decreasing rotational constraint with increasing \mathcal{R} leads to decreasing effect of Ekman
 330 pumping on the velocity and temperature field. Therefore, the difference between r.m.s.
 331 velocity and temperature magnitudes with no-slip and free-slip conditions diminish with
 332 increasing \mathcal{R} . We find LSV in the regime of geostrophic turbulence for FS cases (see tables
 333 2-3 and section 3.4 for details). With this flow structure, the horizontal velocity becomes
 334 higher than all the other cases.

335

336 Apart from the velocity and thermal fields, we look into the effect of boundary conditions on
 337 the enstrophy, relative helicity and the magnetic field. The vertical variations of horizontally
 338 averaged enstrophy, relative helicity, mean and r.m.s. magnetic field strengths are depicted in
 339 figure 3a,b,c and d respectively. In turbulent dynamos, the dynamical alignment of magnetic
 340 field lines (Tobias 2021) occurs around the edges of vortices. A measure of the strength of
 341 the vortical elements in the flow is given by the Enstrophy $E_\omega = 1/2 \overline{\omega_i \omega_i}$. The strength of
 342 the vortices can decide the extent to which they can deform the magnetic field lines around
 343 them, and therefore can be correlated with the local Lorentz force magnitude (Naskar & Pal
 344 2022). The vorticity fluctuations are enhanced in the bulk, as depicted by the enstrophy, with
 345 more than two orders of magnitude jump near the boundaries (see the inset in figure 3a). The
 346 strength of the vortices are enhanced due to Ekman pumping near the wall. The presence of
 347 the energetic vortices near the wall may significantly alter the boundary layer dynamics and

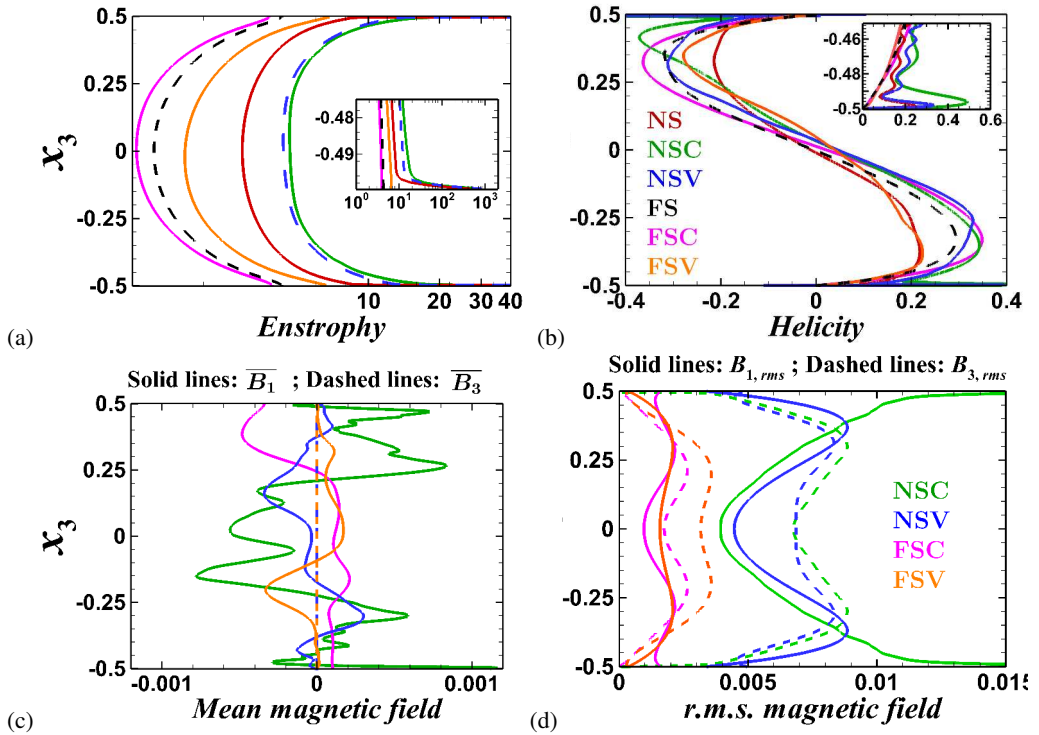


Figure 3: Vertical variation of the r.m.s. quantities: (a) entrophy, (b) relative helicity, (c) mean magnetic field, (d) r.m.s. magnetic field at $\mathcal{R} = 3$. All the quantities are averaged in time and in the horizontal directions.

348 the associated heat transfer characteristics of a dynamo compared to the same without the
 349 presence of Ekman layer with free-slip boundaries (Naskar & Pal 2022). Another important
 350 quantity is the kinetic helicity of the flow, which can induce large-scale mean fields in a
 351 dynamo (Tilgner 2012). The relative kinetic helicity $\mathcal{H}_r = \overline{u_i \omega_i} / 2 (KE_\omega)^{1/2}$, exhibit the
 352 well-known spatial segregation in the vertical direction, as expected in RC, with negative and
 353 positive helicity dominating in the bottom and top halves of the domain respectively (Cattaneo
 354 & Hughes 2006; Schmitz & Tilgner 2010). Helicity is enhanced by the presence of the wall,
 355 where the thermal plumes departing from the boundary layer towards the bulk are spun up
 356 by the Coriolis force, due to Ekman pumping (Schmitz & Tilgner 2010). This phenomenon
 357 results in a strong correlation between local velocity and vorticity that leads to a peak of
 358 relative kinetic helicity near the wall, as shown in the inset in figure 3b. However, in the bulk,
 359 the relative helicity magnitude remains similar for all the dynamo simulations. Additionally,
 360 we look into the effect of boundary conditions on the strength and structure of the magnetic
 361 field produced by the dynamos. The horizontally averaged mean magnetic field is plotted in
 362 figure 3c, which illustrates the dependence on magnetic boundary conditions, even in the
 363 bulk. NSC conditions lead to the highest mean field magnitude among all the cases. It should
 364 be noted here that for perfectly conducting boundaries the vertical component of the mean
 365 magnetic field, $\overline{B_3}$, is identically zero by the definition of averages 2.9 and the solenoidal
 366 field condition 2.1, so that the mean field remains horizontal. Conversely, the mean field is
 367 three-dimensional with purely vertical field at the boundaries for pseudo-vacuum conditions.
 368 However, at $\mathcal{R} = 3$ the mean vertical field remains small compared to the horizontal field
 369 for NSV and FSV conditions in figure 3c. We find that the vertical average of B_1 and B_2 is

370 two orders of magnitude smaller than the maximum mean field strength for NSC and FSC
 371 boundary conditions. Jones & Roberts (2000) also analytically demonstrates that for perfectly
 372 conducting boundaries, the vertical averages of the mean magnetic fields are zero. However,
 373 NSV and FSV boundaries do not satisfy this condition. The fluctuating part of the magnetic
 374 is always three-dimensional, with all components non-zero except at the wall. The r.m.s.
 375 value of the fluctuating horizontal and vertical magnetic fields are plotted in figure 3d. For
 376 $\mathcal{R} = 3$, the fluctuating magnetic field is approximately one order of magnitude stronger than
 377 the mean magnetic field. However, lower thermal forcing can generate strong, large-scale
 378 mean magnetic fields as reported in earlier studies (Stellmach & Hansen 2004; Tilgner 2012;
 379 Naskar & Pal 2022). Dynamos with no-slip boundary conditions lead to higher r.m.s. field
 380 strength than that with free-slip boundaries. For NSC conditions, a large horizontal r.m.s.
 381 field magnitude can be observed near the boundaries. The stretching of the magnetic field
 382 lines by the strong vortices near the wall results in an increase in the r.m.s. field strength.
 383 As the magnetic field has to remain parallel to a perfectly conducting surface, it remains
 384 trapped near the walls, leading to a build-up of the magnetic field strength (St Pierre 1993).
 385 Recently, the DNS of Kolhey *et al.* (2022) has confirmed this build-up of the field for
 386 NSC conditions that creates a stringent resolution requirement near the boundaries. Overall
 387 structure and magnitude of the magnetic field, both in the bulk and near the boundaries,
 388 are strongly dependent on the combination of kinematic and magnetic boundary conditions
 389 for all \mathcal{R} . The traditional Elsasser number, $\Lambda_{lr} = \sigma B_\tau^2 / 2\rho\Omega = 2RaEMPr_m / Pr$ provides
 390 a non-dimensional measure of the magnetic field strength, where $M = 1/2\langle B_i B_i \rangle$ is the
 391 volume-averaged magnetic energy and $B_\tau = \sqrt{\rho\mu u_f (2M)^{1/2}}$ is a characteristic value of
 392 the magnetic field. As reported in tables 1-4, the magnetic field strength of the dynamos
 393 monotonically rises with increasing thermal forcing for all boundary conditions. However,
 394 the relative mean-field strength \overline{M}/M , where $\overline{M} = 1/2\langle B_i \rangle \langle B_i \rangle$, is found to decrease (tables
 395 1-4) with increasing \mathcal{R} , indicating a shift towards small-scale dynamo action with increasing
 396 thermal forcing (Tilgner 2012, 2014). We find "energetically robust" dynamos at $\mathcal{R} = 2$
 397 (corresponding to $\overline{Re}_m = Re_m E^{1/3} = O(1)$) with significant \overline{M}/M confirming the findings
 398 of Yan & Calkins (2022b). The present study shows that such dynamos are generated for
 399 $\overline{Re}_m \approx O(1)$, irrespective of the boundary conditions.

400

3.2. Force balance

401 Now we look into the dynamical balances of the dynamos with different kinematic
 402 and magnetic boundary conditions at $\mathcal{R} = 3$. Figure 4 shows the vertical variation of
 403 the horizontally averaged forces, evaluated from the r.m.s. values of each terms in the
 404 momentum equation 2.2 (Yan *et al.* 2021; Guzmán *et al.* 2021). The first and second
 405 columns in this figure present the forces for no-slip and free-slip boundary conditions
 406 respectively, at $\mathcal{R} = 3$. Here, the RC simulation results (first row) are used as a reference
 407 to interpret the results for DC simulations with perfectly conducting (second row) and
 408 pseudo-vacuum (third row) boundary conditions. At $\mathcal{R} = 3$, we get the thermal and Ekman
 409 boundary layer thickness as $\delta_T = 0.011$ and $\delta_E = 0.002$ for the no-slip cases, whereas
 410 the thermal layer thickness increases to $\delta_T = 0.034$ for the free-slip cases. The near-wall
 411 regions are magnified in the insets, with the velocity and thermal boundary layer edges
 412 marked by the black horizontal dashed and dash-dot lines respectively, in figure 4a. For all
 413 the cases shown in this figure, the leading-order balance between Coriolis and pressure force
 414 indicates a geostrophic state in the bulk. For non-magnetic rapid RC, geostrophic balance
 415 in the bulk has been confirmed by DNS (Guzmán *et al.* 2021), apart from reduced-order
 416 models in the rapidly rotating limit (Julien *et al.* 2012b). The DNS study of rapidly
 417 rotating DC by Yan & Calkins (2022a) has also found leading-order geostrophic balance,

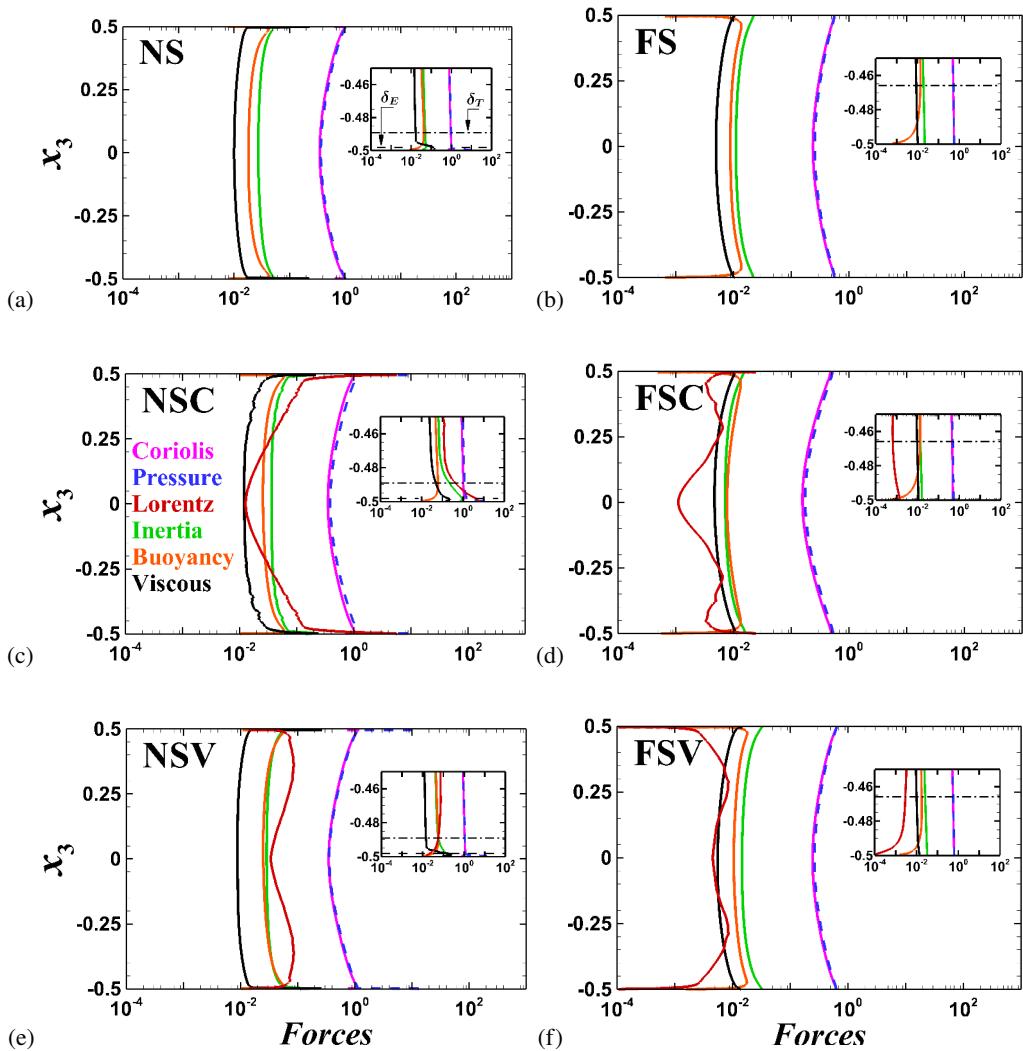


Figure 4: Vertical variation of forces for (a) NS, (b) FS, (c) NSC, (d) FSC, (e) NSV, (f) FSV cases at $\mathcal{R} = 3$. The horizontally averaged force distribution is shown in the bulk and near the bottom plate (inset).

418 for FSV conditions. Departure from the geostrophic state due to the other forces, which
 419 constitute a lower order quasi-geostrophic balance, makes turbulent convection possible.
 420 In the non-magnetic simulations (NS and FS) in figures 4a and b, the geostrophic and
 421 quasi-geostrophic forces behave similarly except near the boundaries (see insets), where
 422 viscous force break the geostrophic balance and dominate the other quasi-geostrophic forces
 423 (inertia and buoyancy) in the Ekman layer near the plates with the no-slip boundary condition.
 424

425 For the dynamo simulations, the Lorentz force exerted by the magnetic field on the flow
 426 also enters the quasi-geostrophic balance. For the NSC case, as shown in figure 4c, the
 427 Lorentz force is minimum at the mid-plane, which increases towards the walls to dominate
 428 the quasi-geostrophic balance for $x_3 \leq -0.25$. Inside the thermal boundary layer, the

429 Lorentz force increases to the same order of magnitude as the Coriolis force, and eventually
430 becomes the highest force at the wall. This is reflected by the value of the local Elsasser
431 number, Λ_T (the ratio of the r.m.s. magnitudes of the Lorentz and the Coriolis forces at
432 the edge of the thermal boundary layer, calculated from the horizontally averaged variation
433 of the two forces), as presented in the tables 1-4. This increase in the Lorentz force at the
434 thermal boundary layer edge leads to a local magnetorelaxation of the thermal boundary
435 layer, which results in increased turbulence and heat transport (Naskar & Pal 2022). Similar
436 behaviour of the Lorentz force near the boundary was found in the range $\mathcal{R} = 3 - 5$ for
437 the NSC cases. However, no such enhancement of Lorentz force is found in the dynamo
438 simulations with any other combinations of the boundary conditions. For the NSV case
439 in figure 4e, the Lorentz force is higher than the other quasi-geostrophic forces in the
440 bulk, but decreases inside the thermal layer. Unlike the NSC case, the Lorentz force in the
441 NSV case keeps decreasing towards the Ekman layer, where the viscous force dominates.
442 The volume-averaged ratio of the Lorentz and the Coriolis force Λ_V is also presented in
443 tables 1-4. This volume-averaged Elsasser number reaches a maximum near $\mathcal{R} = 4$ for the
444 NSV case in table 2. The Lorentz force inside the thermal layer is one order of magnitude
445 smaller than the other quasi-geostrophic forces for the FSC case in figure 4d, making the
446 near-wall balance similar to the non-magnetic RC (FS). Though the Lorentz force has similar
447 magnitude with the viscous force in the bulk for the FSV cases in figure 4f, it becomes the
448 smallest force inside the thermal boundary layer, again making the balance similar to the FS
449 case near the walls. Therefore, our results corroborates the finding of Yan & Calkins (2022a),
450 that the Lorentz force act as a small perturbation in the force balance, with similar magnitude
451 to the viscous force, for the FSV boundaries. These results illustrate the dependence of the
452 dynamical balance of the dynamo on the imposed boundary conditions, especially near the
453 boundary. Also, the dynamo simulations with no-slip conditions exhibit distinctive balance
454 compared to the non-magnetic convection inside the thermal boundary layer. In contrast, the
455 dynamical balance in the thermal layer is similar to RC for free-slip boundary conditions
456 with negligible contribution from the Lorentz force. The magnetic boundary condition
457 decide the magnitude and vertical distribution of the Lorentz force in the dynamos.

458
459 The force balance in the NSC case at $\mathcal{R} = 3$ exhibits some interesting features near the
460 boundary layer as shown in figure 4. This case can be analyzed in more detail from figure 5,
461 where the horizontal and vertical balances are illustrated separately and compared with the
462 NS case. As the rotation axis is aligned with the vertical, the Coriolis force acts only in the
463 horizontal planes, whereas the buoyancy force is purely vertical. In the non-magnetic NS
464 case, the leading-order horizontal balance is geostrophic between the Coriolis and pressure
465 forces as depicted in figure 5a. The ageostrophy, as defined by the difference between the two
466 forces, is balanced by the inertia and viscous forces. Near the walls, there is a sharp increase
467 in the ageostrophy, balanced by the viscous force, indicating a loss of geostrophic balance
468 inside the viscous boundary layers, as seen in the inset of figure 5a (see also (Guzmán *et al.*
469 2021)). Among the vertical forces in figure 5b, the vertical pressure gradient is balanced by
470 the inertia and buoyancy forces in the bulk where the viscous forces remain small.

471
472 In the NSC case, the leading-order balance remains geostrophic in the horizontal direction
473 as presented in figure 5c. However, the ageostrophy is much higher than the NS case due to
474 magnetorelaxation of the Taylor-Proudman theorem in the presence of Lorentz force. The
475 ageostrophic component is balanced by the Lorentz and the inertial forces in the bulk. In the
476 vertical direction, the pressure force is balanced by the Lorentz, buoyancy, and inertial forces
477 as shown in figure 5d. We note here that the horizontal components of the forces are always
478 higher than the vertical forces with the force magnitudes enhanced near the boundaries for

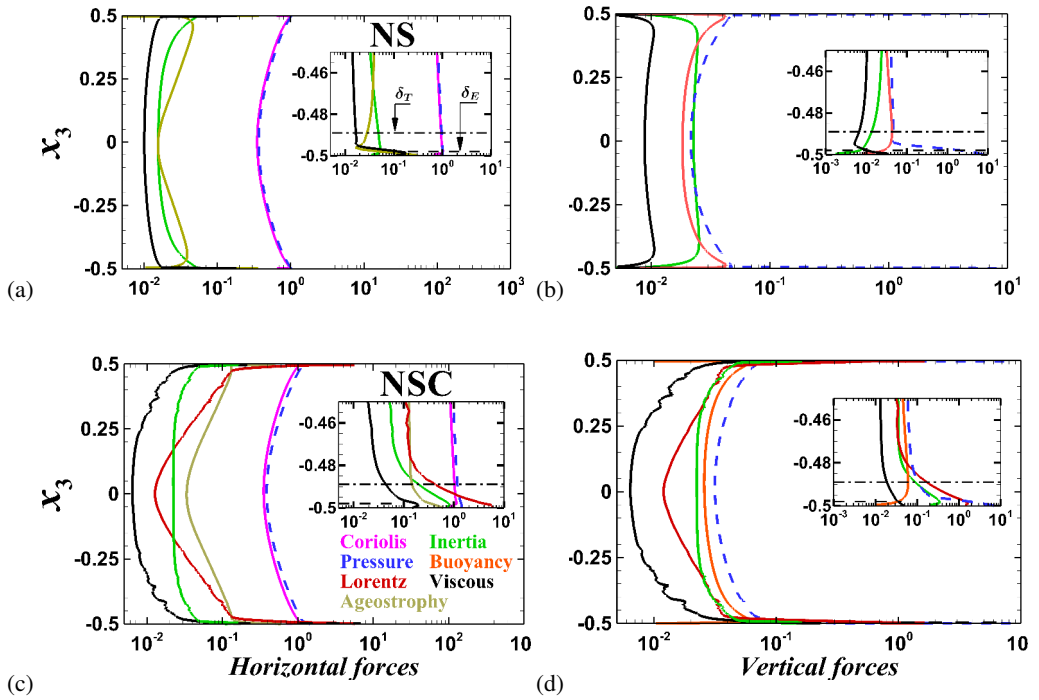


Figure 5: Vertical variation of the force components for (a,b) NS and (c,d) NSC cases.

Horizontal component of the forces $F_h = \sqrt{F_{x_1}^2 + F_{x_2}^2}$ are shown in left column while their vertical components (F_{x_3}) are in the right column. Horizontally averaged force distribution is shown here at $\mathcal{R} = 3$ both in the bulk, and near the bottom plate (inset)

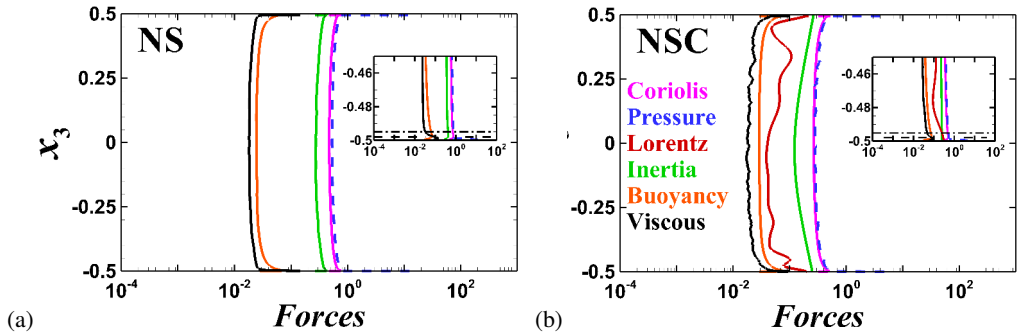


Figure 6: Vertical profiles of the forces for (a) NS, (b) NSC cases at $\mathcal{R} = 20$. The horizontally averaged force distribution is shown in the bulk and near the bottom plate(inset).

479 all the cases. The flow velocities gradually come to zero inside the Ekman layer, resulting
 480 in an increase in the pressure at the boundary. Furthermore, the details of the force balance,
 481 especially the role of inertia in the force balance, depend on \mathcal{R} . With increase in \mathcal{R} , the
 482 inertial force eventually dominates the quasi-geostrophic balance as observed for $\mathcal{R} = 20$
 483 in figure 6a and b for NS and NSC cases respectively. This increase in inertia with thermal
 484 forcing corroborates the findings of Guzmán *et al.* (2021), and a common feature among all
 485 boundary conditions. The local magnetorelaxation of the rotational constraint in the thermal

16

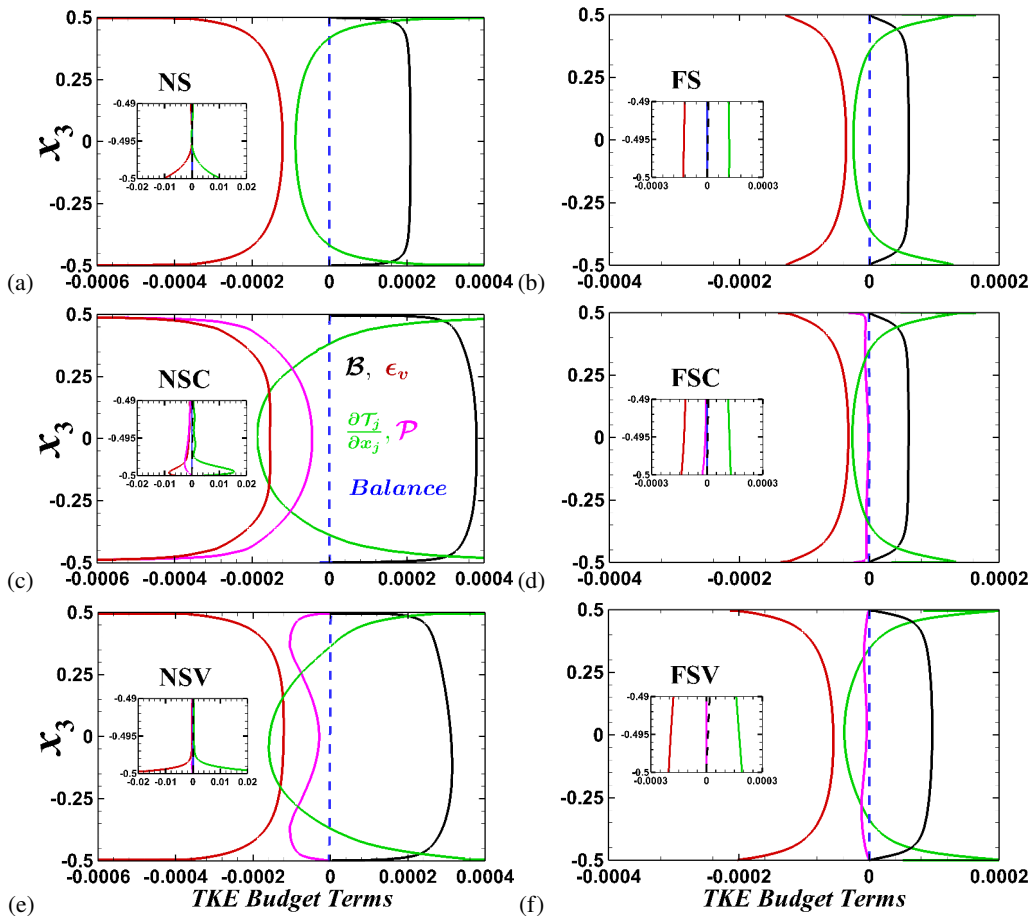


Figure 7: Vertical variation of t.k.e. budget terms at $\mathcal{R} = 3$ for both no-slip (a, c, e) and free-slip (b, d, f) boundaries. Energy budget terms are presented for non-magnetic simulations (a, b) as well as dynamo simulations with both conducting (c, d) and pseudo-vacuum (e, f) conditions. The horizontally averaged budget terms in equation A 1 are averaged in time. The profiles near the bottom wall are magnified in the insets. The balance term signify the difference between left and right hand sides of equation A 1, and indicates sufficient accuracy of the present calculations.

486 boundary layer, as a mechanism for increase in heat transfer in NSC case compared to NS
 487 case, becomes gradually ineffective with increasing \mathcal{R} . This is because of the increased
 488 inertia, rather than the Lorentz force breaks the Taylor-Proudman constraint for both RC and
 489 DC simulations, irrespective of boundary conditions.

490

3.3. Energy Budget

491 We further analyze the various energetic terms in the t.k.e. budget equation A 1 to illustrate
 492 the generation of t.k.e. from thermal forcing, its dissipation and conversion to magnetic
 493 energy for elucidating the turbulent dynamo mechanism. The significance of the t.k.e. budget
 494 terms and their dependence on the boundary conditions has been explored, with a particular
 495 attention to the near-wall features. In figure 7, the various terms in the t.k.e. budget equation
 496 (see appendix A) are plotted with the near-wall variation shown in the inset. All the terms
 497 are averaged in the horizontal planes, and their variation in the vertical direction is shown

498 at $\mathcal{R} = 3$ with varying boundary conditions. For NS and FS cases, in figure 7a and b, the
 499 primary energy balance is between the buoyant production (\mathcal{B}) and viscous dissipation (ϵ_v).
 500 The transport term $\partial\mathcal{T}_j/\partial x_j$ acts to redistribute the energy and becomes zero when averaged
 501 over the volume. This term includes the combined effect of diffusive transport, pressure
 502 transport, and third-order correlation terms (see equation A3). A detailed discussion of a
 503 typical energy budget in RC with the individual treatment of these terms can be found in
 504 Kunnen *et al.* (2009). In the absence of a mean flow, the shear production term, P , is zero,
 505 whereas the unsteady term $\partial K/\partial t$ also becomes zero in the statistically stationary state.
 506 In the bulk, for the non-magnetic RC cases (as shown in figures 7a and b), some part of
 507 the t.k.e. generated from the buoyant production is converted to thermal energy by viscous
 508 dissipation, and the rest is redistributed by the transport term. Near the boundaries, this
 509 transport of kinetic energy term transfers energy from the bulk towards the boundary layers,
 510 which undergoes viscous dissipation. Hence, the primary balance is between the dissipation
 511 and transport terms near the plates. Due to the presence of viscous Ekman layers in the NS
 512 case, the viscous dissipation (and therefore the kinetic energy transport) increases by two
 513 orders of magnitude near the plates compared to their bulk values, as shown in the inset of
 514 figure 7a. Such an order of magnitude jump is not present for the FS case in figure 7b owing
 515 to the absence of the Ekman boundary layer.
 516

517 For the dynamos, the magnetic production of t.k.e. (\mathcal{P}) appears in A1 to represent the
 518 work done by the Lorentz force on the velocity field to produce t.k.e. A negative value
 519 of this term indicates transfer of energy from the velocity field to the magnetic field and
 520 vice-versa. This term is responsible for converting some part of the kinetic energy to
 521 magnetic energy to sustain dynamo action. For all the dynamo cases (NSC, NSV, FSC,
 522 and FSV), \mathcal{P} appears as an additional sink of t.k.e. that balances the buoyant production of
 523 kinetic energy together with viscous dissipation. The behaviour of magnetic production is
 524 similar to viscous dissipation for the NSC case. Here, the budget terms show a peak near
 525 the edge of the Ekman layer as shown in the inset of figure 7c. For NSV boundary condition
 526 in figure 7e, the magnetic production term is not significant near the midplane but increases
 527 towards the boundary to reach a peak near $x = \pm 0.4$ before it decreases to zero at the wall.
 528 For FSC and FSV conditions, the contribution from this term is not significant to the overall
 529 budget as plotted in figures 7d and f. This magnetic production term in the t.k.e. budget
 530 comprises of three components \mathcal{P}_1 , \mathcal{P}_2 and \mathcal{P}_3 as expressed in equation A4. Out of these, the
 531 first two magnetic production terms involving the mean magnetic field and its gradients (\mathcal{P}_1
 532 and \mathcal{P}_2) are found to be small compared to \mathcal{P}_3 at $\mathcal{R} = 3$. It should be noted here that for lower
 533 convective supercriticality, the mean magnetic field may become strong compared to the
 534 turbulent magnetic field, and therefore the terms \mathcal{P}_1 and \mathcal{P}_2 may significantly contribute to
 535 magnetic production. The transport of kinetic energy by the mean and fluctuating magnetic
 536 fields, as represented by the last two terms in the RHS of equation A3, are also found to be
 537 small compared to the pressure transport and turbulent transport terms (figure not presented).
 538

539 The dominant term among the magnetic production terms, \mathcal{P}_3 , represents the work done by
 540 the fluctuating magnetic field on the fluctuating velocity field to produce t.k.e. It is interesting
 541 to study this term for elucidating the mechanism of energy exchange between these two
 542 vector fields. The nine components of this term are represented by $\mathcal{P}_3^{ij} = \overline{B'_i B'_j \partial u'_i / \partial x_j}$ in
 543 figure 8 for NSC and NSV cases where magnetic production makes significant contribution
 544 to the t.k.e. budget. Among these nine components, the three terms involving the vertical
 545 gradient of the fluctuating velocity field, $\mathcal{P}_3^{i3} = \overline{B'_i B'_3 \partial u'_i / \partial x_3}$ where $i = 1, 2, 3$, are small
 546 due to Taylor-Proudman constraint on the velocity field imposed by rotation that suppresses

18

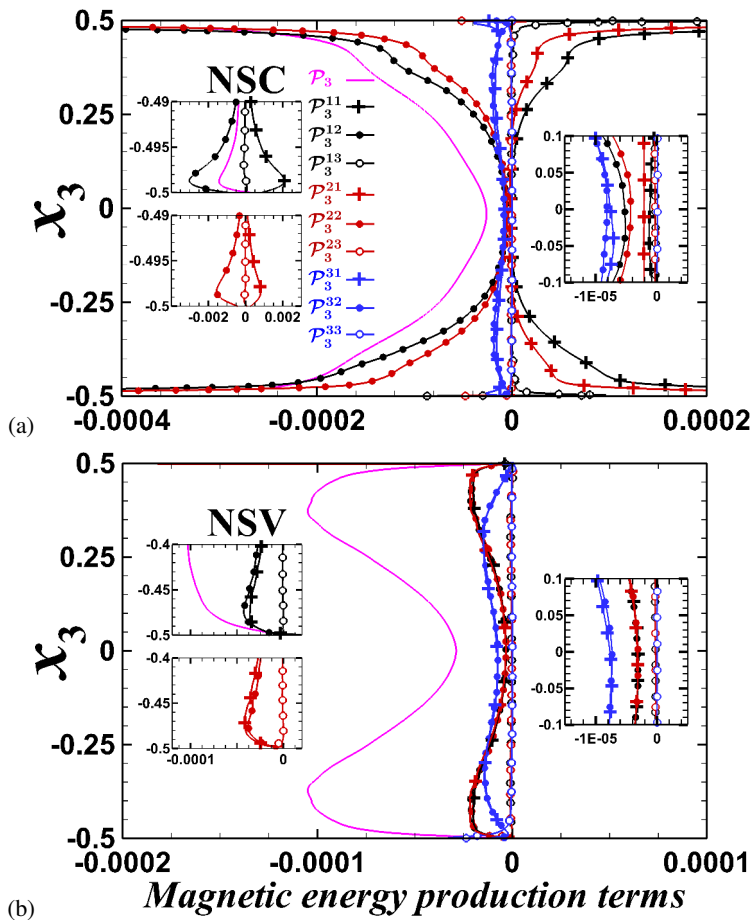


Figure 8: Variation of the magnetic production terms for (a) NSC and (b) NSV case at $\mathcal{R} = 3$. The components of the work done by the Lorentz force \mathcal{P}_3 , are represented by the colors black for $i = 1$, red for $i = 2$ and blue for $i = 3$. Here the lines with + symbols, lines with filled and open circles represent $j = 1$, $j = 2$ and $j = 3$ respectively.

547 changes in the vertical direction. Interestingly, for the NSC case, there are components with
 548 both positive and negative values in figure 8a. Here, the components \mathcal{P}_3^{11} and \mathcal{P}_3^{21} become
 549 positive away from the midplane, indicating a transfer of energy from the magnetic field to
 550 the velocity field. Vertical variation of the terms \mathcal{P}_3^{12} and \mathcal{P}_3^{22} are similar but opposite, with
 551 negative values away from the mid-plane indicating transfer of energy from the velocity to
 552 the magnetic field. The last two negative terms, being larger than the positive terms, provide
 553 a bias in the direction of energy transfer so that the system can extract kinetic energy of the
 554 fluid and convert it to magnetic energy to sustain dynamo action. However, at the mid-plane,
 555 all the terms are negative. Near the wall, these four terms exhibit peaks near the edge of
 556 the Ekman boundary layer where the values are two orders of magnitude higher than the
 557 mid-plane. The two remaining terms \mathcal{P}_3^{31} and \mathcal{P}_3^{32} are small compared to the dominant terms
 558 near the wall but contribute most to the energy transfer at the midplane. In the NSV case, all
 559 the components of work done by Lorentz force \mathcal{P}_3^{ij} are negative, indicating unidirectional
 560 energy transfer from the velocity field to the magnetic field. This indicates that the imposed
 561 boundary conditions dictate the energy exchange mechanism between the velocity and

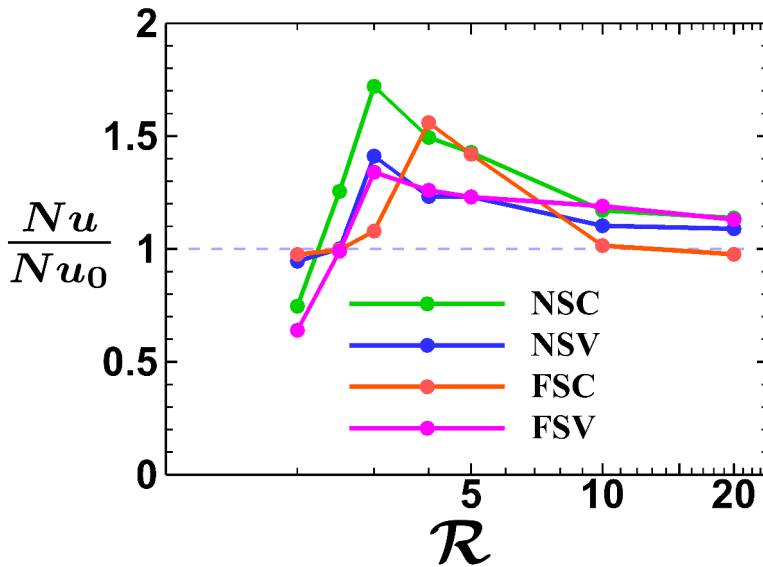


Figure 9: Variation of Nusselt number ratio Nu/Nu_0 as a function of the thermal forcing for different boundary conditions. Here Nu_0 represents the Nusselt number for the non-magnetic RC simulations.

562 magnetic fields, both in the bulk and near the boundaries.

563

564 The volume-averaged budget of turbulent magnetic energy, reduces to a balance between
 565 the magnetic energy production and the Joule dissipation, $\langle \mathcal{P} \rangle = \langle \epsilon_j \rangle$, for statistically
 566 stationary turbulence. This signifies that the part of t.k.e. converted to magnetic energy,
 567 ultimately converts to thermal energy via Joule dissipation. The ohmic fraction, defined by
 568 the ratio of Joule dissipation to total dissipation $\langle \epsilon_j \rangle / \langle \epsilon \rangle$, is presented in tables 1-4. The
 569 ohmic fraction does not show any particular trend in the range $\mathcal{R} = 2 - 20$. The global energy
 570 balance between buoyant production $\langle \mathcal{B} \rangle$ and total dissipation $\langle \epsilon \rangle$ is also presented in these
 571 tables, where the values have been scaled by a factor of 10^4 . The difference between the two
 572 terms never exceeds 5% of $\langle \mathcal{B} \rangle$ indicating the accuracy of the present DNS in capturing
 573 all the energy containing scales. The vertical trends of the terms in t.k.e. equation remains
 574 similar to that presented in figure 7 over the range of thermal forcing studied here. The
 575 volume-averaged buoyancy flux and dissipation increases by an order of magnitude in the
 576 range $\mathcal{R} = 2 - 20$.

577

578

3.4. Heat transfer behaviour

579 Finally, we study the heat transfer behaviour of the dynamo simulations with increasing
 580 thermal forcing under the influence of different boundary conditions. In figure 9, the Nusselt
 581 number ratio, Nu/Nu_0 , signifies the change in heat transport in DC simulations due to
 582 dynamo action compared to the non-magnetic RC simulations. For NSC, a peak is found
 583 near $\mathcal{R} = 3$ with more than 72% enhancement in heat transfer. A peak in Nusselt number
 584 ratio is also found for the NSV case at $\mathcal{R} = 3$, with a 41% increase in heat transport
 585 compared to non-magnetic RC. For FSC and FSV cases, the heat transfer ratio also peaks at
 586 $\mathcal{R} = 4$ and $\mathcal{R} = 3$ with enhancement up to 56% and 34% respectively. The ratio of viscous
 587 dissipation in the DC and RC simulations $\langle \epsilon_v \rangle / \langle \epsilon_0 \rangle$ is also presented in the table, which

20

588 shows a similar trend with the Nusselt number ratio. The peaks in heat transfer ratio and the
 589 viscous dissipation ratio occurs at the same value of \mathcal{R} . We note here that the overall energy
 590 balance of the system leads to an exact relation between the Nusselt number and the total
 591 dissipation, $Nu = 1 + \sqrt{RaPr}\langle\epsilon\rangle$. Hence the dissipation ratio should behave similarly as the
 592 Nusselt number ratio with varying \mathcal{R} as seen in the tables 1-4. A local magnetorelaxation
 593 of the rotational constraint, due to enhanced Lorentz force in the thermal boundary layer
 594 (see figure 4c), has been proposed to be the reason for the rise in heat transfer in the
 595 NSC case (Naskar & Pal 2022). However, the build-up of the Lorentz force required for
 596 this magnetorelaxation process is not present for any other combinations of the boundary
 597 conditions (see figure 4). Notably, in the NSV case, the Lorentz force in the bulk is higher
 598 compared to the other cases in figure 4e. Indeed, the volume-averaged Elsasser number,
 599 Λ_V in table 2 shows a peak at $\mathcal{R} = 3$ that correlates well with the heat transfer behaviour.
 600 Therefore, the global relaxation of the Taylor-Proudman constraint is a possible mechanism
 601 for the heat transfer enhancement. For the free-slip cases, the heat transfer enhancement in
 602 dynamos is achieved by suppression of LSV by the small-scale magnetic field, as discussed
 603 in the next paragraph. It is interesting to note that the peak in heat transfer ratio appears
 604 within a narrow range of thermal forcing $\mathcal{R} = 3 - 4$ depending on the conditions at the
 605 boundary. Further investigations will be necessary to elucidate the appearance of the peak in
 606 heat transfer ratio for different boundary conditions. However, the heat transport properties
 607 of the dynamo depend on the boundary conditions and the associated dynamical balances
 608 both in the bulk and in the boundary layer.

609

610 The heat transfer enhancement in the dynamos with free-slip boundary conditions with
 611 respect to non-magnetic RC can be attributed to the absence of LSV in the former. In the FS
 612 cases, we find the presence of depth-independent, long-lived (compared to the free-fall time
 613 scale) LSV for $\mathcal{R} \geq 4$, corroborating the findings of Guervilly *et al.* (2014). Similar to freely
 614 decaying 2D turbulence, the formation of LSV in RC involves an upscale energy transfer
 615 from the convective eddies to large-scale barotropic modes (Favier *et al.* 2014; Rubio *et al.*
 616 2014). The flow associated with these structures are nearly 2D, that can be visualized from
 617 the contours of horizontal t.k.e., $K_h = 1/2(u_1^2 + u_2^2)$, which tends to be high in the shear
 618 layer around the core of these vortices as shown in figure 10a for $\mathcal{R} = 4$. An animation
 619 of the LSV, as visualized by the time evolution of the K_h contours, can be found in the
 620 supplementary video. Here, we find a pair of cyclonic and anti-cyclonic vortices centered
 621 around (0.48, 0.87) and (0.93, 0.34) respectively as depicted in the horizontal mid-plane
 622 at $x_3 = 0.5$. The degree to which the two-dimensionality of the flow has been induced by
 623 the presence of an LSV can be measured by the ratio $\tau = \langle u_1^2 + u_2^2 + u_3^2 \rangle / 3\langle u_3^2 \rangle$, as reported
 624 in the tables 1-4. The kinetic energy ratio for the RC simulations τ_0 is also reported in the
 625 tables 2 and 3 for NS and FS cases respectively. As the kinetic energy associated with the
 626 horizontal flow in the LSV is higher than the kinetic energy in the vertical flow, the value of
 627 τ increase to values much higher than unity in the FS cases for $\mathcal{R} \geq 4$. We have also found
 628 LSV with no-slip boundary conditions without magnetic field (NS case) for $\mathcal{R} = 10$ and 20,
 629 which supports the findings of Guzmán *et al.* (2020), that LSV appear in RC irrespective of
 630 the kinematic boundary condition. However, the presence of no-slip boundaries suppresses
 631 the formation of LSV until higher convective supercriticality ($\mathcal{R} \geq 10$) compared to the
 632 free-slip cases ($\mathcal{R} \geq 4$).

633

634 Guervilly *et al.* (2017) reported that, for $Re_m \geq 550$, the formation of LSV can be
 635 suppressed by the presence of a small-scale magnetic field. Such a field acts to disrupt the
 636 correlations between the convective vortices that in turn hinders the upscale transfer of

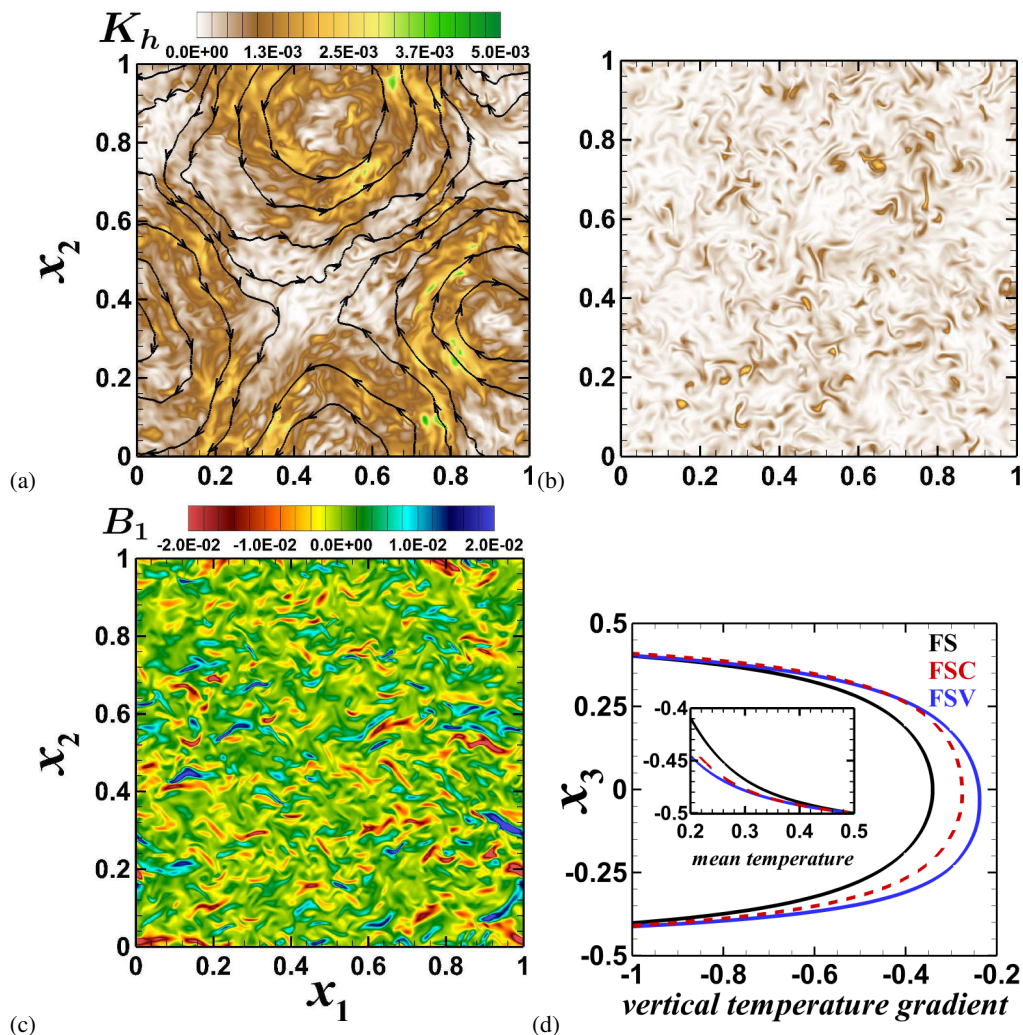


Figure 10: Contours of horizontal t.k.e., $K_h = 1/2(u_1^2 + u_2^2)$ for (a) FS and (b) FSC cases at $\mathcal{R} = 4$. The instantaneous plots are shown in the horizontal mid-plane at $x_3 = 0.5$ to illustrate the presence of LSV in (a) FS which is superimposed with streamlines. The dynamo simulation with FSC conditions generates small scale velocity and magnetic fields as illustrated by contours of t.k.e. and magnetic field B_1 in (b) and (c) respectively. The vertical temperature gradients at $\mathcal{R} = 4$ are shown in (d) for the free-slip cases. The mean temperature profile near the lower wall is also shown in the inset.

637 energy. This should be the reason that we do not find any LSV in our dynamo simulations
 638 with free-slip conditions that operate for $Re_m \geq 641$. The combined effect of the no-slip
 639 boundary condition and the presence of magnetic field has suppressed the LSV in the NSC
 640 and NSV cases as well, as reflected by the value of τ in table 1 and 2. Maffei *et al.* (2019)
 641 used an asymptotic magnetohydrodynamic model to study the effect of an imposed magnetic
 642 field on the inverse cascade of energy in the turbulent geostrophic regime of RC. The
 643 possibility of occurrence of LSV in the presence of the magnetic field was quantified by an
 644 interaction parameter N , which signifies the relative strengths of the Lorentz force and the
 645 non-linear advection. For $N \geq 0.013$ the magnetic field disrupts the upscale energy transfer,

646 and hence LSV can only be present below this limit. We have calculated the interaction
647 parameter as a ratio of the volume-averaged r.m.s. magnitudes of the Lorentz force and
648 the non-linear advection terms, and found the ratio to be of $O(10^{-1})$ for all our dynamo
649 simulations. Though the self-excited magnetic fields in our dynamo simulations are not
650 directly comparable to the externally imposed field used by Maffei *et al.* (2019), the magnetic
651 quenching of the inverse cascade is a plausible mechanism for the disappearance of LSV in
652 our dynamo simulations. The horizontal t.k.e. and the x_1 -component of the magnetic field for
653 FSC cases, as depicted in figure 10b and c, shows small-scale fields without any trace of LSV.
654 The presence of LSV can disrupt the vertical mixing by transferring energy to horizontal
655 barotropic modes (Guervilly *et al.* 2014). In figure 10d, this phenomenon results in an
656 increased gradient of temperature in the bulk for the FS case with LSV, compared to the FSC
657 and FSV cases without LSV. The temperature profiles near the wall (see inset) shows higher
658 thermal boundary layer thickness in the FS case compared to the dynamo cases, indicating
659 a decrease in heat transfer efficiency near the wall in the FS case. The thermal plumes near
660 the wall get swept away by the horizontal flow associated with LSV, which can interrupt
661 the vertical transport of heat by the plumes, leading to a decrease in the heat transfer efficiency.
662

663 4. Conclusions

664 We have performed high fidelity DNS of dynamos driven by rapidly rotating RBC under
665 four combinations of kinematic and magnetic boundary conditions. The simulations are
666 performed in the rotation dominated regime $\mathcal{R} = 2 - 20$ at a fixed rotation rate $E = 5 \times 10^{-7}$
667 and fluid properties $Pr = Pr_m = 1$. The dynamo simulations with the no-slip and free-slip
668 kinematic boundary conditions combined with the perfectly conducting and pseudo-vacuum
669 magnetic boundary conditions (NSC, NSV, FSC, and FSV) are compared against non-
670 magnetic simulations (NS and FS) to study the impact of the dynamo action on the
671 convective flow properties. Our previous study (Naskar & Pal 2022) reported the existence
672 of optimal heat transfer enhancement with respect to non-magnetic convection due to
673 dynamo action for NSC boundary conditions at $\mathcal{R} = 3$. Therefore, we have chosen this
674 case to compare the statistics of the velocity, thermal and magnetic fields in addition to the
675 dynamical balance, energy budget, and the heat transfer behaviour of the dynamos.
676

677 The flow and thermal field of the dynamos, apart from the structure of the magnetic field,
678 are found to depend on the boundary conditions. Ekman pumping significantly enhances
679 the velocity and thermal fluctuations in the dynamos, increasing the r.m.s. velocities and
680 temperatures both in the bulk and near the boundaries. It also leads to a three orders of
681 magnitude increase in enstrophy, signifying increased strength of the vortical plumes inside
682 the Ekman layer with the no-slip boundary condition. The relative helicity also exhibits a
683 peak near the Ekman layer, illustrating strong correlations between the velocity and vorticity
684 fields. The perfectly conducting boundary conditions can trap the magnetic field near the
685 boundaries to prevent its escape and make it purely horizontal. This leads to a jump of r.m.s.
686 horizontal field strength near the boundaries for the NSC case. The r.m.s. field strength
687 remains higher than the mean-field for all combinations of the boundary conditions in the
688 investigated range of thermal forcing.
689

690 The leading-order force balance in the dynamos remains geostrophic, similar to our
691 non-magnetic RC simulations, irrespective of the boundary conditions. At $\mathcal{R} = 3$, the
692 quasi-geostrophic balance corresponds to a CIA balance between the ageostrophic part of
693 Coriolis force, inertia, and buoyancy forces in the non-magnetic simulations. The extent to

694 which the Lorentz force modulates the quasi-geostrophic balance is decided by the boundary
695 conditions in the dynamo simulations. For NSC conditions, a build-up of the Lorentz force
696 is seen near the walls, whereas this force dominates the quasi-geostrophic balance in the bulk
697 for NSV conditions. For free-slip conditions, the Lorentz force is much weaker compared to
698 the no-slip dynamos.

699

700 The budget of t.k.e. for the non-magnetic cases exhibits an overall balance between
701 the buoyant production and viscous dissipation. For the NS case, the viscous dissipation
702 increases by two orders of magnitude from its bulk value due to viscous action inside the
703 Ekman layer. For the dynamo simulations, some part of the t.k.e. is converted to magnetic
704 energy via work done by the Lorentz force, which is ultimately converted to thermal energy
705 by the Joule dissipation. This additional term, signifying the production of magnetic energy
706 in the dynamo simulations, is considerably weaker with free-slip boundaries than no-slip
707 boundaries. A break up of the components that constitute this production of magnetic energy
708 term (which can also be interpreted as the work done by Lorentz force on the flow), reveals
709 that the energy flows both ways, from velocity field to the magnetic field and vice-versa,
710 when NSC conditions are imposed at the boundary. Conversely, the flow of energy is
711 unidirectional, from kinetic energy to magnetic energy, when NSV boundary condition is
712 used, indicating the decisive role of the boundary conditions on the mechanism of energy
713 transfer.

714

715 Another interesting finding of our study is the enhancement of heat transfer in the DC
716 simulations with respect to the non-magnetic RC simulations. The heat transfer enhancement
717 reaches a peak in the range $\mathcal{R} = 3 - 4$ for all the combinations of boundary conditions.
718 The magnetorelaxation of the rotational constraint by the Lorentz force is the mechanism
719 for heat transfer enhancement for the no-slip cases, whereas, for the free-slip dynamos,
720 the suppression of LSV by magnetic field is found to be the reason behind the increased
721 efficiency of heat transport. We have found the LSV in our non-magnetic simulations that
722 are known to deteriorate the heat transfer, as reported in literature (Guervilly *et al.* 2014).
723 By comparing our results with existing literature, we conclude that the magnetic quenching
724 of LSV by the magnetic field is a possible reason for the heat transfer enhancement in our
725 free-slip dynamo simulations. An interesting extension of the present study will be the
726 search for power-law scaling of the heat transfer and flow speed with the thermal forcing in
727 such convection-driven dynamos and the effect of boundary conditions on the power-law
728 exponent and the prefactor.

729

730 Finally, we would like to point out that the near wall force balance and the heat transfer
731 behaviour of rotating DC should also depend on Pr , along with the boundary conditions.
732 The length scale at which the Lorentz force enters the force balance (Schwaiger *et al.* 2019;
733 Aurnou & King 2017), apart from its dependence on Pr_m (if any), also warrants future
734 investigations.

735 **Supplementary data.** A Supplementary movie of Large scale vortex is available at
736 https://doi.org/**.***jfm.***...

737 **Acknowledgements.** We gratefully acknowledge the support of the Science and Engineering Research
738 Board, Government of India grant no. SERB/ME/2020318. We also want to thank the Office of Research
739 and Development, Indian Institute of Technology Kanpur for the financial support through grant no.
740 IITK/ME/2019194. The support and the resources provided by PARAM Sanganak under the National
741 Supercomputing Mission, Government of India at the Indian Institute of Technology, Kanpur are gratefully
742 acknowledged.

743 **Declaration of interests.** The authors report no conflict of interest.

24

744 **Author contributions.** The authors contributed equally to analysing data and reaching conclusions, and in
745 writing the paper.

746 **Appendix A.**

747 The t.k.e. equation for a rapidly rotating dynamo can be derived by including the terms
748 involving work done by the Lorentz force. We note here that the Coriolis force is a pseudo
749 force and does not enter the balance directly. The evolution of the horizontally averaged t.k.e.
750 (see section 3.1 for the definition of the averages), can be written as the following.

$$751 \quad \frac{dK}{dt} = -P + \mathcal{B} - \epsilon_v - \frac{\partial \mathcal{T}_j}{\partial x_j} + \mathcal{P} \quad (\text{A } 1)$$

752 where,

$$754 \quad K = \frac{1}{2} \overline{u'_i u'_i}, \quad P = -\overline{u'_i u'_j} \frac{\partial \bar{u}_i}{\partial x_j}, \quad \mathcal{B} = \overline{u'_3 \theta'}, \quad \epsilon_v = \sqrt{\frac{Pr}{Ra}} \frac{\partial u'_i}{\partial x_j} \frac{\partial u'_i}{\partial x_j}; \quad (\text{A } 2)$$

755 are the t.k.e., shear production, buoyancy flux and the viscous dissipation. The transport
756 of K is given below

$$757 \quad \mathcal{T}_j = \overline{u'_j p'} + \frac{1}{2} \overline{u'_i u'_i u'_j} - \sqrt{\frac{Pr}{Ra}} \frac{\partial^2 K}{\partial x_j \partial x_j} - \bar{B}_j \overline{u'_i B'_i} - \overline{u'_i B'_i B'_j} \quad (\text{A } 3)$$

758 The shear production term P in equation A 2 is negligible in the absence of a mean flow in
759 the present simulations. However, shear production may still arise in the presence of a mean
760 vertical motion through the turbulent transport term in equation A 3 (Kerr 2001). The last
761 term in the RHS of equation A 1 is the production of K due to the work done by the Lorentz
762 force on the flow field.

$$763 \quad \mathcal{P}_1 = -\bar{B}_j \overline{B'_i \frac{\partial u'_i}{\partial x_j}}; \quad \mathcal{P}_2 = \overline{u'_i B'_j} \frac{\partial \bar{B}_i}{\partial x_j}; \quad \mathcal{P}_3 = -\overline{B'_i B'_j} \frac{\partial u'_i}{\partial x_j}; \quad \mathcal{P} = \mathcal{P}_1 + \mathcal{P}_2 + \mathcal{P}_3 \quad (\text{A } 4)$$

764 These magnetic production terms \mathcal{P}_1 to \mathcal{P}_3 in equation A 4 represent the exchange of
765 energy between the velocity and the magnetic fields. For example, \mathcal{P}_1 signify the production
766 of t.k.e. due to work done by the mean magnetic field on the fluctuating strain rate of the
767 velocity field. Furthermore, \mathcal{P}_2 represents the production of t.k.e. due to mean magnetic field
768 gradient, analogous to the shear production term P in A 2. The amplification (or attenuation)
769 of the magnetic energy, due to the work done by stretching (or squeezing) of magnetic field
770 lines by the fluctuating velocity gradients, is represented by the term \mathcal{P}_3 . The terms \mathcal{P}_1
771 and \mathcal{P}_2 , apart from the last two terms in equation A 3, representing the transport of kinetic
772 energy by the magnetic field, remains small except at $\mathcal{R} = 2$.

773

REFERENCES

- 774 AURNOU, J.M. & KING, E.M. 2017 The cross-over to magnetostrophic convection in planetary dynamo
775 systems. *Proc. R. Soc. Lond. A Math Phys. Sci.* **473** (2199), 20160731.
776 AURNOU, J. M., BERTIN, V., GRANNAN, A. M., HORN, S. & VOGT, T. 2018 Rotating thermal convection in
777 liquid gallium: multi-modal flow, absent steady columns. *J. Fluid Mech.* **846**, 846–876.
778 AURNOU, J. M., HORN, S. & JULIEN, K. 2020 Connections between nonrotating, slowly rotating, and rapidly
779 rotating turbulent convection transport scalings. *Phys. Rev. Res.* **2** (4), 043115.

- 780 BRUCKER, K.A. & SARKAR, S. 2010 A comparative study of self-propelled and towed wakes in a stratified
781 fluid. *J. Fluid Mech.* **652**, 373–404.
- 782 CALKINS, M.A. 2018 Quasi-geostrophic dynamo theory. *Phys. Earth Planet. Inter.* **276**, 182–189.
- 783 CALKINS, M.A., JULIEN, K., TOBIAS, S.M. & AURNOU, J.M. 2015 A multiscale dynamo model driven by
784 quasi-geostrophic convection. *J. Fluid Mech.* **780**, 143–166.
- 785 CATTANEO, F. & HUGHES, D.W. 2006 Dynamo action in a rotating convective layer. *J. Fluid Mech.* **553**,
786 401–418.
- 787 CHANDRASEKHAR, S. 1961 *Hydrodynamic and hydromagnetic stability*. Courier Corporation.
- 788 CHENG, J. S., MADONIA, M., GUZMÁN, A. J. A. & KUNNEN, R. P. J. 2020 Laboratory exploration of heat
789 transfer regimes in rapidly rotating turbulent convection. *Phys. Rev. Fluids.* **5** (11), 113501.
- 790 CHENG, J. S., STELLMACH, S., RIBEIRO, A., GRANNAN, A., KING, E. M. & AURNOU, J. M. 2015 Laboratory-
791 numerical models of rapidly rotating convection in planetary cores. *Geophys. J. Int.* **201** (1), 1–17.
- 792 CHILDRESS, S. & SOWARD, A. M. 1972 Convection-driven hydromagnetic dynamo. *Phys. Rev. Lett.* **29** (13),
793 837.
- 794 CNOSSEN, I. 2014 The importance of geomagnetic field changes versus rising CO_2 levels for long-term
795 change in the upper atmosphere. *J. Space Weather Space Clim.* **4**, A18.
- 796 ECKE, ROBERT E & NIEMELA, JOSEPH J 2014 Heat transport in the geostrophic regime of rotating rayleigh-
797 bénard convection. *Phys. Rev. Lett.* **113** (11), 114301.
- 798 ERDMANN, W., KMITA, H., KOSICKI, J. Z. & KACZMAREK, Ł 2021 How the geomagnetic field influences life
799 on earth—an integrated approach to geomagnetobiology. *Orig. Life Evol. Biosph.* pp. 1–27.
- 800 FAUTRELLE, Y. & CHILDRESS, S. 1982 Convective dynamos with intermediate and strong fields. *Geophys.*
801 *Astrophys. Fluid Dyn.* **22** (3–4), 235–279.
- 802 FAVIER, BENJAMIN, SILVERS, LJ & PROCTOR, MRE 2014 Inverse cascade and symmetry breaking in rapidly
803 rotating boussinesq convection. *Physics of Fluids* **26** (9), 096605.
- 804 GUERVILLY, C., HUGHES, D.W. & JONES, C.A. 2015 Generation of magnetic fields by large-scale vortices
805 in rotating convection. *Phys. Rev. E.* **91** (4), 041001.
- 806 GUERVILLY, C., HUGHES, D.W. & JONES, C.A. 2017 Large-scale-vortex dynamos in planar rotating
807 convection. *J. Fluid Mech.* **815**, 333–360.
- 808 GUERVILLY, C., HUGHES, D. W. & JONES, C. A. 2014 Large-scale vortices in rapidly rotating rayleigh–bénard
809 convection. *J. Fluid Mech.* **758**, 407–435.
- 810 GUZMÁN, A. J. A., MADONIA, M., CHENG, J. S., OSTILLA-MÓNICO, R., CLERCX, H. J. H. & KUNNEN, R.
811 P. J. 2020 Competition between ekman plumes and vortex condensates in rapidly rotating thermal
812 convection. *Phys. Rev. Lett.* **125** (21), 214501.
- 813 GUZMÁN, A. J. A., MADONIA, M., CHENG, J. S., OSTILLA-MÓNICO, R., CLERCX, H. J. H. & KUNNEN, R.
814 P. J. 2021 Force balance in rapidly rotating rayleigh–bénard convection. *J. Fluid Mech.* **928**.
- 815 IYER, K.P., SCHEEL, J.D., SCHUMACHER, J. & SREENIVASAN, K.R. 2020 Classical $1/3$ scaling of convection
816 holds up to $Ra = 10^{15}$. *Proc. Natl. Acad. Sci. USA* **117** (14), 7594–7598.
- 817 JONES, C.A. & ROBERTS, P.H. 2000 Convection-driven dynamos in a rotating plane layer. *J. Fluid Mech.*
818 **404**, 311–343.
- 819 JULIEN, K., AURNOU, J. M., CALKINS, M. A., KNOBLOCH, E., MARTI, P., STELLMACH, S. & VASIL, G. M.
820 2016 A nonlinear model for rotationally constrained convection with ekman pumping. *J. Fluid Mech.*
821 **798**, 50–87.
- 822 JULIEN, KEITH, KNOBLOCH, EDGAR, RUBIO, ANTONIO M & VASIL, GEOFFREY M 2012a Heat transport in
823 low-rossby-number rayleigh–bénard convection. *Phys. Rev. Lett.* **109** (25), 254503.
- 824 JULIEN, K., LEGG, S., McWILLIAMS, J. & WERNE, J. 1996 Rapidly rotating turbulent rayleigh–bénard
825 convection. *J. Fluid Mech.* **322**, 243–273.
- 826 JULIEN, K., RUBIO, A.M., GROOMS, I. & KNOBLOCH, E. 2012b Statistical and physical balances in low
827 Rossby number Rayleigh–Bénard convection. *Geophys. Astrophys. Fluid Dyn.* **106** (4–5), 392–428.
- 828 KERR, R.M. 2001 Energy budget in Rayleigh–Bénard convection. *Phys. Rev. Lett.* **87**, 244502–1–244502–4.
- 829 KING, E.M., STELLMACH, S. & AURNOU, J.M. 2012 Heat transfer by rapidly rotating Rayleigh–Bénard
830 convection. *J. Fluid Mech.* **691**, 568–582.
- 831 KING, E.M., STELLMACH, S., NOIR, J., HANSEN, U. & AURNOU, J.M. 2009 Boundary layer control of rotating
832 convection systems. *Nature* **457** (7227), 301–304.
- 833 KING, E. M. & AURNOU, J. M. 2013 Turbulent convection in liquid metal with and without rotation. *Proc.*
834 *Natl. Acad. Sci. USA* **110** (17), 6688–6693.

- 835 KOLHEY, P., STELLMACH, S. & HEYNER, D. 2022 Influence of boundary conditions on rapidly rotating
836 convection and its dynamo action in a plane fluid layer. *Phys. Rev. Fluids*. **7** (4), 043502.
- 837 KUNNEN, R.P.J., GEURTS, B.J. & CLERCX, H.J.H. 2009 Turbulence statistics and energy budget in rotating
838 Rayleigh–Bénard convection. *Eur. J. Mech. B Fluids* **28** (4), 578–589.
- 839 KUNNEN, R. P. J. 2021 The geostrophic regime of rapidly rotating turbulent convection. *J. Turbul.* **22** (4-5),
840 267–296.
- 841 KUNNEN, R. P. J., GEURTS, B. J. & CLERCX, H. J. H. 2010 Experimental and numerical investigation of
842 turbulent convection in a rotating cylinder. *J. Fluid Mech.* **642**, 445–476.
- 843 KUNNEN, R. P. J., OSTILLA-MÓNICO, R., VAN DER POEL, E. P., VERZICCO, R. & LOHSE, D. 2016 Transition
844 to geostrophic convection: the role of the boundary conditions. *J. Fluid Mech.* **799**, 413–432.
- 845 MAFFEI, S., CALKINS, M. A., JULIEN, K. & MARTI, P. 2019 Magnetic quenching of the inverse cascade in
846 rapidly rotating convective turbulence. *Phys. Rev. Fluids*. **4** (4), 041801.
- 847 MAFFEI, S., KROUSS, M. J., JULIEN, K. & CALKINS, M. A. 2021 On the inverse cascade and flow speed
848 scaling behaviour in rapidly rotating rayleigh–bénard convection. *J. Fluid Mech.* **913**.
- 849 MENEGUZZI, M. & POUQUET, A. 1989 Turbulent dynamos driven by convection. *J. Fluid Mech.* **205**,
850 297–318.
- 851 MOFFATT, K. & DORMY, E. 2019 *Self-exciting fluid dynamos*. Cambridge University Press.
- 852 NASKAR, S. & PAL, A. 2022 Direct numerical simulations of optimal thermal convection in rotating plane
853 layer dynamos. *J. Fluid Mech.* **942**, A37.
- 854 NIEVES, DAVID, RUBIO, ANTONIO M & JULIEN, KEITH 2014 Statistical classification of flow morphology in
855 rapidly rotating rayleigh–bénard convection. *Phys. Fluids* **26** (8), 086602.
- 856 PAL, ANIKESH 2020 Deep learning emulation of subgrid-scale processes in turbulent shear flows. *Geophys.*
857 *Res. Lett.* **47** (12), e2020GL087005.
- 858 PAL, A. & CHALAMALLA, V.K. 2020 Evolution of plumes and turbulent dynamics in deep-ocean convection.
859 *J. Fluid Mech.* **889**, A35.
- 860 PAL, A. & SARKAR, S. 2015 Effect of external turbulence on the evolution of a wake in stratified and
861 unstratified environments. *J. Fluid Mech.* **772**, 361–385.
- 862 PAL, A., DE STADLER M.B. & S., SARKAR 2013 The spatial evolution of fluctuations in a self-propelled wake
863 compared to a patch of turbulence. *Phys. Fluids* **25**, 095106.
- 864 PLUMLEY, M. & JULIEN, K. 2019 Scaling laws in Rayleigh-Benard convection. *Earth and Space Science*
865 **6** (9), 1580–1592.
- 866 PLUMLEY, M., JULIEN, K., MARTI, P. & STELLMACH, S. 2016 The effects of ekman pumping on quasi-
867 geostrophic rayleigh–bénard convection. *J. Fluid Mech.* **803**, 51–71.
- 868 PLUMLEY, M., JULIEN, K., MARTI, P. & STELLMACH, S. 2017 Sensitivity of rapidly rotating rayleigh–bénard
869 convection to ekman pumping. *Phys. Rev. Fluids*. **2** (9), 094801.
- 870 RUBIO, A. M., JULIEN, K., KNOBLOCH, E. & WEISS, J. B. 2014 Upscale energy transfer in three-dimensional
871 rapidly rotating turbulent convection. *Phys. Rev. Lett.* **112** (14), 144501.
- 872 RÜDIGER, G. & HOLLERBACH, R. 2006 *The magnetic universe: geophysical and astrophysical dynamo*
873 *theory*. John Wiley & Sons.
- 874 SCHMITZ, S. & TILGNER, A. 2010 Transitions in turbulent rotating rayleigh–bénard convection. *Geophys.*
875 *Astrophys. Fluid Dyn.* **104** (5-6), 481–489.
- 876 SCHWAIGER, T., GASTINE, T. & AUBERT, J. 2019 Force balance in numerical geodynamo simulations: a
877 systematic study. *Geophys. J. Int.* **219** (Supplement_1), S101–S114.
- 878 SOWARD, A. M. 1974 A convection-driven dynamo i. the weak field case. *Philos. T. Roy. Soc. London A*
879 **275** (1256), 611–646.
- 880 ST PIERRE, M.G. 1993 The strong field branch of the Childress-Soward dynamo. In *Solar and Planetary*
881 *Dynamos* (ed. M.R.E. Proctor & A.D. Gilbert), pp. 245–277. Cambridge University Press.
- 882 STELLMACH, S. & HANSEN, U. 2004 Cartesian convection driven dynamos at low Ekman number. *Phys.*
883 *Rev. E.* **70** (5), 056312.
- 884 STELLMACH, S., LISCHPER, M., JULIEN, K., VASIL, G., CHENG, J.S., RIBEIRO, A., KING, E.M. & AURNOUR,
885 J.M. 2014 Approaching the asymptotic regime of rapidly rotating convection: boundary layers versus
886 interior dynamics. *Phys. Rev. Lett.* **113** (25), 254501.
- 887 TARDUNO, J. A. 2018 Subterranean clues to the future of our planetary magnetic shield. *Proc. Natl. Acad.*
888 *Sci. USA* **115** (52), 13154–13156.
- 889 THELEN, J.-C. & CATTANEO, F. 2000 Dynamo action driven by convection: the influence of magnetic
890 boundary conditions. *Mon. Not. R. Astron. Soc.* **315** (2), L13–L17.

- 891 TILGNER, A. 2012 Transitions in rapidly rotating convection driven dynamos. *Phys. Rev. Lett.* **109** (24),
892 248501.
- 893 TILGNER, A. 2014 Magnetic energy dissipation and mean magnetic field generation in planar convection-
894 driven dynamos. *Phys. Rev. E.* **90** (1), 013004.
- 895 TOBIAS, S. M. 2021 The turbulent dynamo. *J. Fluid Mech.* **912**.
- 896 TOBIAS, S. M., CATTANEO, F. & BOLDYREV, S. 2012 MHD dynamos and turbulence. In *Ten Chapters in*
897 *Turbulence* (ed. P.A. Davidson, Y. Kaneda & K.R. Sreenivasan), pp. 351–404. Cambridge University
898 Press.
- 899 WEISS, S., STEVENS, R. J. A. M., ZHONG, J.-Q., CLERCX, H. J. H., LOHSE, D. & AHLERS, G. 2010 Finite-size
900 effects lead to supercritical bifurcations in turbulent rotating rayleigh-bénard convection. *Phys. Rev.*
901 *Lett.* **105** (22), 224501.
- 902 YAN, M. & CALKINS, M. A. 2022a Asymptotic behaviour of rotating convection-driven dynamos in the
903 plane layer geometry. *arXiv preprint arXiv:2202.01382* .
- 904 YAN, M. & CALKINS, M. A. 2022b Strong large scale magnetic fields in rotating convection-driven dynamos:
905 The important role of magnetic diffusion. *Phys. Rev. Res.* **4** (1), L012026.
- 906 YAN, M., TOBIAS, S.M. & CALKINS, M.A. 2021 Scaling behaviour of small-scale dynamos driven by
907 Rayleigh–Bénard convection. *J. Fluid Mech.* **915**.